https://doi.org/10.5194/egusphere-2026-2988
Preprint. Discussion started: 5 June 2026

Topographic control of tides in the Ross Sea: eddy-like structures, bottom-trapped waves, and energetics

Yue Xia[1], Hengling Leng[2], Zhaomin Wang[2], Craig Stevens[3,4], Chengyan Liu[2], Liangjun Yan[5], Xianxian Han[5], Dake Chen[2,6]

[1]School of Atmospheric Sciences, Sun Yat-sen University, and Southern Marine Science and Engineering Guangdong Laboratory (Zhuhai), Zhuhai, China.
[2]Southern Marine Science and Engineering Guangdong Laboratory (Zhuhai), Zhuhai, China.
[3]Earth Sciences New Zealand, Wellington, New Zealand.
[4]Dept. Physics, Univ. Auckland, Auckland, New Zealand.
[5]School of Marine Sciences, Sun Yat-sen University, Zhuhai, China.
[6]State Key Laboratory of Satellite Ocean Environment Dynamics, Second Institute of Oceanography, Ministry of Natural Resources, Hangzhou, China.

Correspondence to: Hengling Leng (lenghengling@sml-zhuhai.cn)

Abstract. Using a regional high-resolution coupled ocean-sea ice-ice shelf model, this study investigates tide-topography interactions, energy conversions, and tide-induced cross-slope exchange in the Ross Sea. The model resolves tidal time series and power spectral density that agree well with available mooring data. Through tidal decomposition of modelled tides, we identify a diurnal topographic mode along the Ross Sea slope, characterized by three eddy-like structures. These structures arise because the varying topography of the continental slope induces divergence and convergence in the diurnal surface-mode tidal flows. This generates sea surface height extremes that persist longer than the time required for geostrophic adjustment, allowing rotating geostrophic flows (i.e., the topographic mode) to develop around them. The topographic mode dominates the water exchange across the slope and yields a net heat transport towards the shelf (~12 TW). The surface and topographic modes can exchange energy with each other, as indicated by alternating positive and negative patches of energy conversion rate with a magnitude reaching 1 W/m². The baroclinic tides in the Ross Sea manifest as bottom-trapped waves over the continental slope and other topographic gradients. The energy of baroclinic tides, primarily converted from the topographic mode, is an order of magnitude smaller than the barotropic tides. The barotropic component accounts for most of the tidal dissipation along the slope (~0.1 W/m²), with a minimal contribution from baroclinic tides. This study identifies tides as an important driver of heat transport onto the Antarctic shelf, which is fundamental for accurately prediction of future Antarctic ice shelf melt and global sea level rise.

1 Introduction

Around Antarctica, tides are a fundamental driver of ocean dynamics. They accelerate the Antarctic Slope Current and contribute to the formation of the Antarctic Slope Front through convergence along the continental slope (Flexas et al., 2015; Stewart et al., 2019). Tides also modulate ice–ocean stress (Si et al., 2022) and drive cross-shelf overturning circulation

(Garreau and Maze, 1992; Pérenne et al., 2000; Stewart et al., 2019). Beneath ice shelves, tidal sea-level fluctuations exert direct stress on the ice base, inducing flexure and promoting iceberg calving (Riedel et al., 1999; Legrésy et al., 2004; Fricker and Padman, 2006). Tidal currents further influence the dynamics of ice streams that feed ice shelves (Doake et al., 2002; Legrésy et al., 2004; Brunt et al., 2010). In addition, tides enhance vertical mixing and turbulence, facilitating upward heat flux and thereby increasing basal melting beneath ice shelves (Macayeal, 1984a; Holland and Jenkins, 1999; Robertson, 2013). Antarctic Bottom Water (AABW), a key component of the global thermohaline circulation (Orsi et al., 1999; Jacobs, 2004), is formed through processes significantly influenced by tides. Tidal currents mix precursor water masses, such as Circumpolar Deep Water (CDW), Antarctic Surface Water (AASW), and Dense Shelf Water (DSW), at the continental shelf break, with mixing intensity modulated by tidal phase, topography, and stratification (Whitworth and Orsi, 2006; Padman et al., 2009). Beyond mixing, tides also facilitate cross-slope exchange of these water masses (Gordon et al., 2004; Ou et al., 2009; Padman et al., 2009; Castagno et al., 2017; Stewart et al., 2018). By suppressing entrainment in DSW overflows, tides promote the formation of colder and denser AABW (Ou et al., 2009; Guan et al., 2009; Han et al., 2024).

As a primary source of AABW, the Ross Sea exhibits complex tidal dynamics. Research on tides in the Ross Sea began in the early 20th century with ship-based measurements (Darwin, 2009). Following the International Geophysical Year (post-1957), tidal observations intensified, culminating in the first synthesized studies (Gilmour et al., 1962). Successive studies using a gravity station network on the Ross ice shelf (Williams and Robinson, 1980) and moored current meters near and on the ice shelf (Pillsbury and Jacobs, 1985) identified both diurnal and semidiurnal constituents, with the diurnal tides being dominant. Subsequent instrument deployments, such as moorings (Gordon et al., 2004; Whitworth and Orsi, 2006), CTDs (Castagno et al., 2017), and GPS stations (Brunt et al., 2010) yielded data that facilitated enhanced analysis of tides in the Ross Sea. Satellite altimetry addressed the sparseness of in situ data, revealing ice shelf flexure in response to oceanic tides (Padman and Fricker, 2002) and enabling the extraction of accurate tidal signals (Ray, 2008). These altimeter data have also been used to develop sophisticated tidal models through data assimilation (Padman et al., 2003; 2018). Given that conducting in situ measurements poses significant logistical challenges, numerical models were developed to simulate tides (Macayeal, 1984b; Padman et al., 2003; Robertson et al., 2003) and to assess their influence on physical processes such as thermohaline circulation (Macayeal, 1984a; Padman et al., 2009; Wang et al., 2010) in the Ross Sea.

Precious works have documented general characteristics of the tides in the Ross Sea. Padman et al. (2003) first mapped barotropic tidal currents and sea surface height (SSH), providing a two-dimensional framework that Robertson (2003; 2005) extended through three-dimensional modeling, characterizing baroclinic tides and their role in mixing. However, these studies did not separate topographically controlled wave modes, such as vorticity waves (Padman et al., 2003) and continental shelf waves (Robertson, 2005), from the underlying tidal Kelvin wave (Robertson, 2005). Such separation is essential for understanding how topography modulates tidal flow. Moreover, while Robertson (2005) identified semi-diurnal constituents as the primary source of baroclinic tides, the studies of D'Asaro and Morison (1992) and Falahat and Nycander (2015) indicate that diurnal tides can also generate internal tides poleward of their critical latitude (~30°), typically as bottom-trapped waves. At present, the generation, distribution, and role of such bottom-trapped waves in the Ross Sea remain unexplored. Moreover,

https://doi.org/10.5194/egusphere-2026-2988
Preprint. Discussion started: 5 June 2026

existing estimates of tidal energy (Müller, 2013; Falahat and Nycander, 2015) rely on global models that may not adequately represent localized bathymetric effects. A comprehensive tidal energy budget analysis specifically focused on the Ross Sea is therefore needed.

This study employs a high-resolution numerical model, combined with tidal decomposition and energy diagnostics, to investigate tide-topography interactions, their associated energy conversions, and their implications for cross-slope exchange in the Ross Sea. The paper is organized as follows: Section 2 describes the numerical model and outlines the procedures for tidal analysis. Section 3 presents tidal characteristics and provides a comprehensive analysis of both tidal dynamics and energetics. Finally, the findings are summarized and discussed in Sect. 4.

2 Methods

2.1 Model Description

This study utilizes a regional coupled ocean-sea ice-ice shelf model of the Ross Sea, developed and validated by Yan et al. (2023), to examine tides in the Ross Sea. The model is based on the Massachusetts Institute of Technology's general circulation model (MITgcm; Marshall et al., 1997), which solves the hydrostatic Navier-Stokes equations on an orthogonal curvilinear grid under the Boussinesq approximation. It incorporates a dynamic-thermodynamic sea ice model (Zhang and Hibler, 1997; Zhang and Rothrock, 2000) and a thermodynamic ice shelf model (Losch et al., 2010).

The model domain, ranging between 86.5°S-60.6°S and 116.9°E-105.9°W, encompasses the Ross Sea with ice shelves and the surrounding open ocean (Fig.1). The computational grid features a quasi-uniform horizontal resolution of 5 km (420 × 520 grid points) and 70 vertical layers, with layer thickness increasing from 10 m at the surface to 600 m at the bottom. The model topography is constructed from the Refined Topography Data Set 2 (Schaffer and Timmermann, 2016) and is represented using a partial cell scheme to minimize artificial flow distortion from stair-step topography approximations. Lateral boundary conditions for ocean and sea ice fields are prescribed at the northern, eastern, and western open boundaries of the model domain. For the ocean, the prescribed velocity, temperature, and salinity are extracted from the monthly mean climatology of the Southern Ocean State Estimate (SOSE; Mazloff et al., 2010; Verdy and Mazloff, 2017). Tidal currents applied at the open boundaries are obtained from the Circum-Antarctic Tidal Simulation (Padman et al., 2002, 2003), which incorporates 10 major tidal constituents (M_f, M_m, K_2, S_2, M_2, N_2, K_1, P_1, O_1, and Q_1). Sea ice boundary conditions, including ice thickness, concentration, velocity, and snow thickness, are obtained from SOSE and the National Snow and Ice Data Center (Fetterer et al., 2017). Atmospheric forcing is derived from the European Centre for Medium-Range Weather Forecasts Reanalysis v5 dataset (ERA5; Hersbach et al., 2023), which offers global meteorological fields with a spatial resolution of 0.25° and temporal resolution of an hour. The details regarding the model configuration and parametrizations have been described by Yan et al. (2023). The model was integrated from 1979 to 2019, with hourly outputs of 2003–2004 saved for analyzing tidal dynamics.

https://doi.org/10.5194/egusphere-2026-2988
Preprint. Discussion started: 5 June 2026

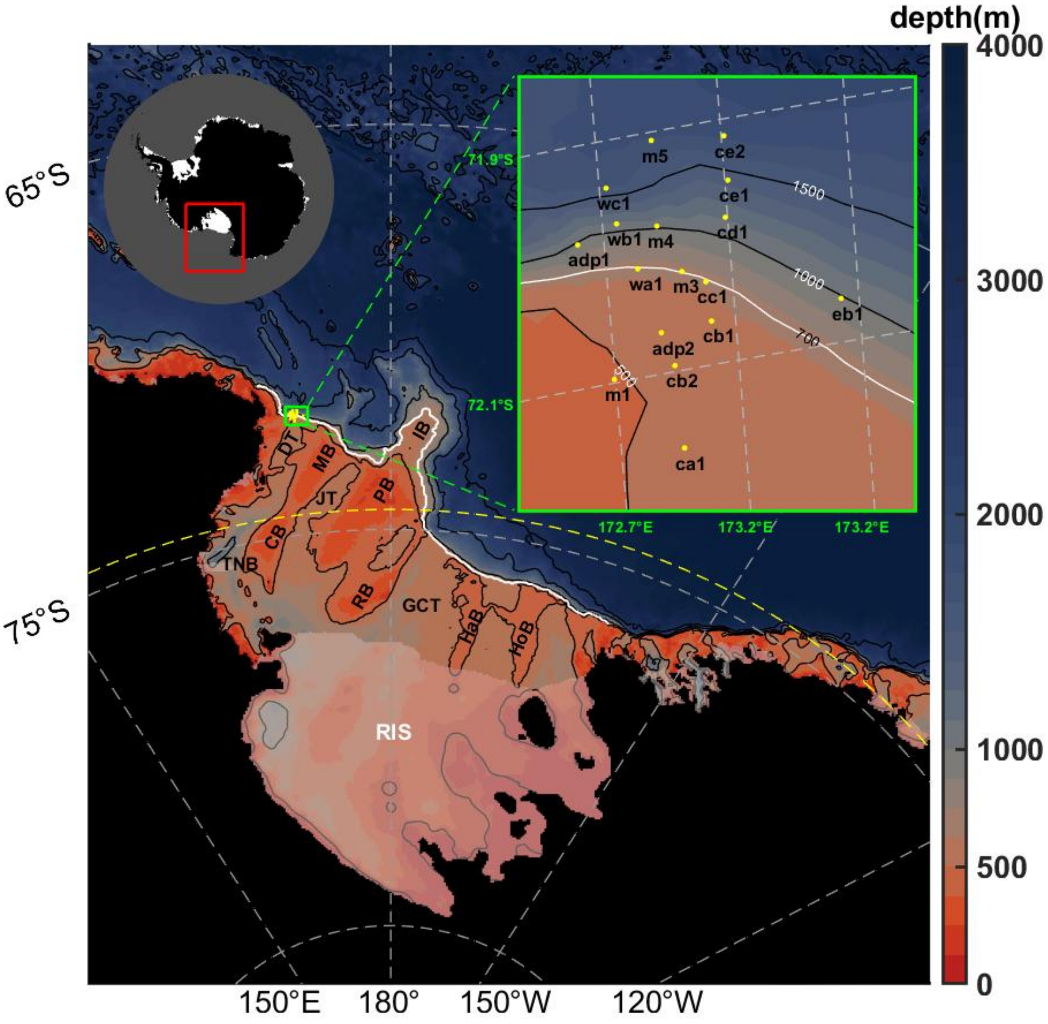

Figure 1. Map of the bathymetry within the model domain (outlined by the red box in the inset). Topographic features are depicted with color shading, and the ice shelves are rendered semi-transparent (DT: Drygalski Trough; JT: Joides Trough; GCT: Glomar Challenger Trough; IB: Iselin Bank; CB: Crary Bank; MB: Mawson Bank; PB: Pennell Bank; RB: Ross Bank; TNB: Terra Nova Bay; HaB: Hayes Bank; HoB: Houtz Bank). The yellow dashed line marks the latitude of 74.5°S. The yellow dots indicate the hydrographic mooring stations from the Antarctic Slope (AnSlope) program, outlined by the green inset box. Bathymetric contours (black lines) are drawn for the 500, 1000, 2000, and 3000-m depths. The white line marks the selected segment of the 700-m isobath on the slope, which is used for subsequent analysis.

2.2 Model Validation

The model's performance in simulating key components, such as sea ice production, water mass properties, and ice shelf melting, was validated by Yan et al. (2023), and its simulation of circulation over the continental shelf and slope was validated by Liu et al. (2025). In this study, we validate the simulated tides in the Ross Sea, by both benchmarking them against previous model studies, and comparing with hydrographic timeseries observations.

https://doi.org/10.5194/egusphere-2026-2988
Preprint. Discussion started: 5 June 2026

For comparison with previous studies, we calculated the two key diagnostic parameters defined by Padman et al. (2002, 2003): the root-sum-square of tidal harmonic amplitude and the time-averaged tidal flow speed. The spatial patterns shown in our Fig. 2 are consistent with those presented in Fig. 2 of Padman et al. (2003), whose results were derived from both "forward" (dynamical) and "inverse" (data assimilation) models.

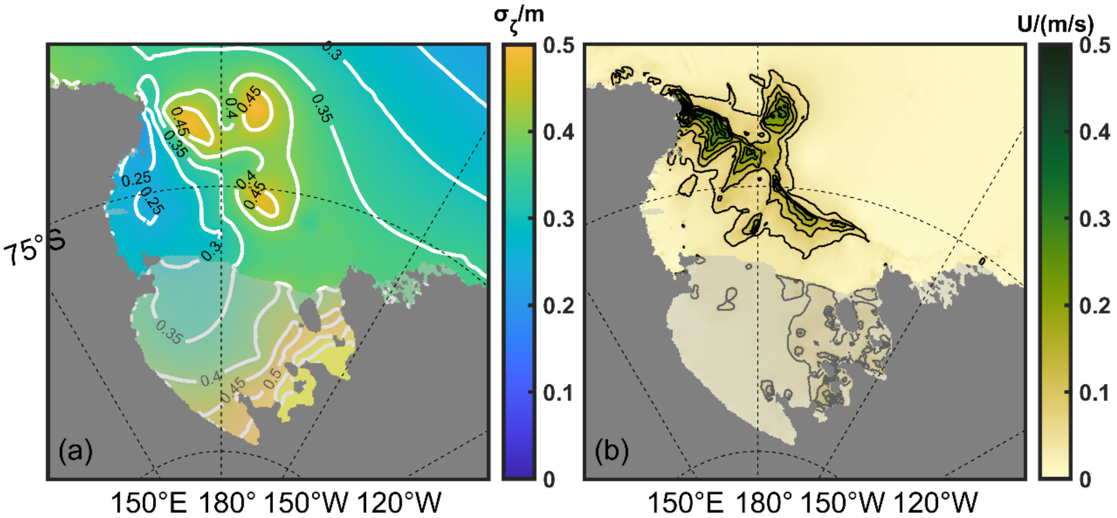

Figure 2. Spatial patterns of tidal characteristics calculated by definitions from Padman et al. (2002, 2003): (a) Root-sum-square of tidal harmonic amplitude $\sigma_\varsigma = \sqrt{\sum a_i}$ (m), where a_i is the amplitude of the i-th tidal harmonic and (b) Time-averaged tidal flow speed $U = <|\mathbf{u}|>$ (m/s), where angle brackets denote time averaging.

The model's performance in simulating tides is further validated by comparing the time series and power spectral density (PSD) of tidal currents between the model output and observational data. The observational data for comparison are from 17 AnSlope mooring stations, which were located at the mouth of DT (yellow dots in Fig. 1) and deployed during different periods spanning from March 2003 to March 2004. For each mooring station, a point-to-point comparison of tidal currents was conducted by matching the deepest observational data point with the nearest model grid cell. For brevity, only the comparison for central mooring station cc1 is presented in the main text (Fig. 3); the results for the remaining 16 moorings are shown in the supplementary material (Figs. S1-S16). Notably, a mismatch is found at station adp1 (Fig. S1), where the observed stronger semidiurnal signal likely stems from the advective effects of the diurnal tides (Bell, 1975), as the slope there may exceed the resolving capability of the model's vertical grid.

As shown in Fig. 3c, the simulated tidal current energy shows peaks at diurnal and semi-diurnal frequencies matching the observations, although its magnitude is somewhat underestimated (especially for the M_f constituent). The good agreement between model and observations in the filtered time series (Figs. 3a and 3b) validates that the model correctly captures the phase of the predominantly diurnal current, and also reproduces the spring-neap cycle well. This lends credibility to studying the tidal dynamics and energetics in the Ross Sea using the model output.

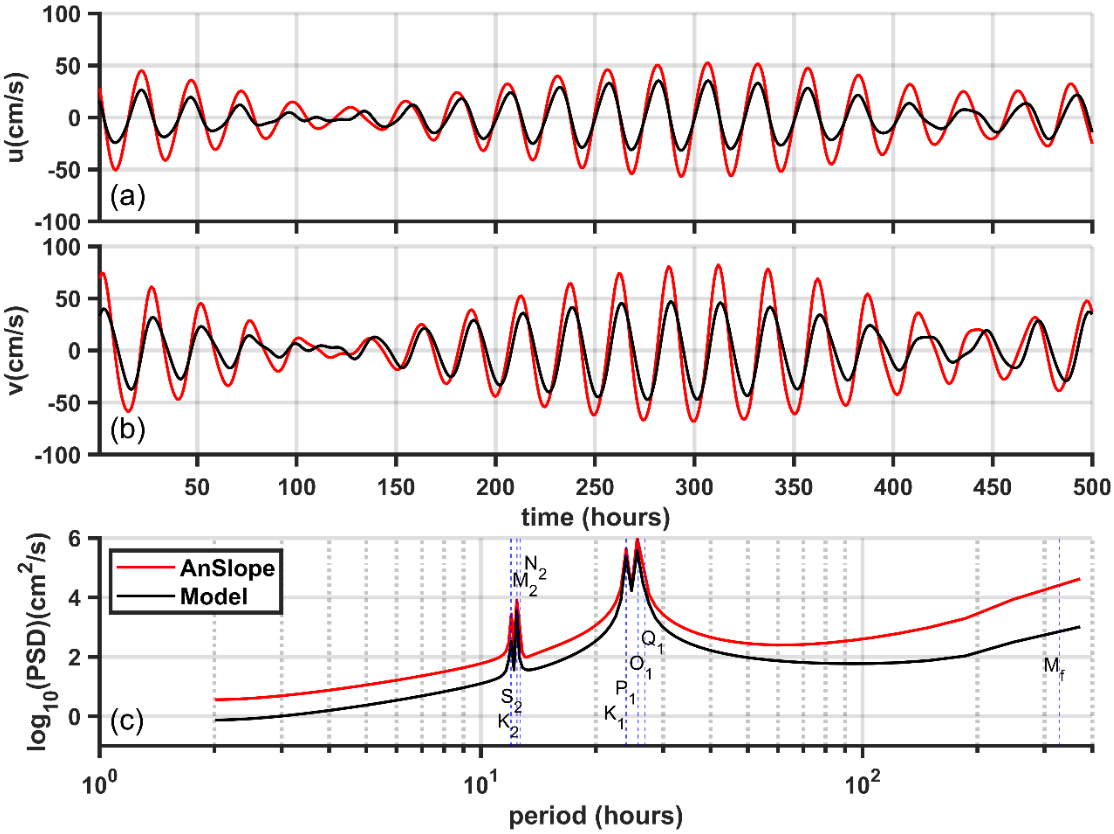

Figure 3. A comparison of the simulated and observed tidal currents at mooring station cc1 (for details, see Table S1 in the Supplementary Material), showing the filtered time series (semi-diurnal and diurnal constituents) of the (a) meridional and (b) zonal 135 **tidal velocities, and (c) the corresponding power spectral density (PSD). The blue dashed lines indicate the periods of the corresponding tidal constituents (labelled adjacent to the lines). Simulated and observed data are shown in black and red, respectively.**

2.3 Extraction of tidal signals

The diversity of oceanic motions in the Ross Sea, which extends beyond tidal signals, necessitates harmonic analysis. However, 140 the computational resources required for the analysis at all model grids are substantial. Combining the Fourier transform and dynamic analysis based on the vorticity equation, Wang et al. (2023) developed an efficient approach to extract wavy motions from full flow. Notably, in regions where the latitude is higher than the critical latitude of the tidal constituent, the wavy motions extracted by their method represent pure tidal signals, whereas at latitudes below the critical latitude, the extracted signals contain not only tidal components but also other wavy features. Since part of the Ross Sea lies below the critical latitude 145 for semi-diurnal tides (~74.5°S, shown by yellow dashed line in Fig.1), a tidal filter following Wang et al. (2023) is used to extract tidal signals:

$$M_{tide}(k,l,\omega) = \begin{cases} 0, & if\ \omega \neq n * \omega_{tide} \quad at\ (k,l,\omega) \\ 1, & if\ \omega = n * \omega_{tide} \quad at\ (k,l,\omega) \end{cases} (n = 1, 2), \tag{1}$$

where k and l denote wavenumbers in the x- and y-directions, and ω_{tide} denotes the frequency of any tidal constituent.

For any physical variable A from the model outputs, the tidal signals can be derived by applying a forward Fourier transform, multiplying the result by a filter function, and subsequently performing an inverse Fourier transform:

$$A_{tide} = F^{-1}(F(A) \times M_{tide}), \tag{2}$$

where F denotes Fourier-transform, F^{-1} the inverse Fourier-transform, and × the multiplication. The extracted signals include both the fundamental tidal constituent (n=1) and its first harmonic (n=2), which is generated by the advective effects of the barotropic tide (Bell, 1975). In this study, the method of Wang et al. (2023) is applied to extract tidal components of both velocity and density perturbations.

2.4 Modal Decomposition of Barotropic Tides

The barotropic tide can be divided into two parts, referred to as the surface mode and the topographic mode, following the framework of Tanaka (2023):

$$\frac{1}{H}\nabla^2\psi_S + \nabla\frac{1}{H}\cdot\nabla\psi_S + J\left(\frac{1}{H},\phi\right) = 0,\ \psi_S = \psi\ at\ boundaries, \tag{3}$$

$$\psi_T = \psi - \psi_S, \tag{4}$$

$$\mathbf{u}_{\boldsymbol{S}} = \frac{1}{H}(\nabla\phi + \mathbf{k}\times\nabla\psi_S), \tag{5}$$

$$\mathbf{u}_{\boldsymbol{T}} = \frac{1}{H}(\mathbf{k}\times\nabla\psi_T), \tag{6}$$

$$C_{S\to T} = \rho_0\psi_T\left[\frac{f}{H}\nabla^2\phi + \nabla\frac{f}{H}\cdot\nabla\phi - J\left(\frac{1}{H},\psi_S\right)\right], \tag{7}$$

where ψ and ϕ are potential and stream functions derived from the Helmholtz decomposition of the depth-integrated transport field, and H is the thickness of water column. $J(a,b) = \frac{\partial a}{\partial x}\frac{\partial b}{\partial y} - \frac{\partial b}{\partial x}\frac{\partial a}{\partial y}$ denotes the Jacobian operator. $\mathbf{u}_{\boldsymbol{S}}$ and $\mathbf{u}_{\boldsymbol{T}}$ are velocity fields associated with the surface and topographic modes, respectively. $C_{S\to T}$ is the energy conversion rate from the surface to the topographic mode.

This decomposition method rests on two key assumptions: (i) SSH variations are entirely attributable to the surface mode (Eq. (5)), and (ii) the topographic mode solely accounts for the relative vorticity (Eq. (6)). Physically, the surface mode corresponds to Kelvin waves, as illustrated by Tanaka (2023). The topographic mode has been attributed to topographic Rossby waves by Tanaka (2023) because topographic Rossby waves are eigenmodes of a continuously stratified coastal ocean with a sloping bottom and a coastal boundary (Wang and Mooers, 1976). Note, however, the continental slope in the Ross Sea is too steep to favor their generation (Han et al., 2024). In this study, the decomposition reveals a topographic mode on the Ross Sea slope, manifested as three eddy-like structures. Unlike propagating Rossby waves, these "eddies" are quasi-stationary and reverse their direction of rotation with the rise and fall of the tide (to be discussed in Sect. 3).

https://doi.org/10.5194/egusphere-2026-2988
Preprint. Discussion started: 5 June 2026

2.5 Energetics analysis

In addition to the barotropic tides, we explore the generation of baroclinic tides and provide a comparative analysis of the energetics associated with both barotropic and baroclinic tidal motions. The barotropic velocity $\mathbf{U}$ and baroclinic velocity $\mathbf{u}'$ are defined as

$$\mathbf{U} = (U, V, 0) = \frac{1}{H}\overline{\mathbf{u}_{\boldsymbol{H}}}, \tag{8}$$

$$\mathbf{u}' = (u', v', w) = \mathbf{u} - \mathbf{U} = (u - U, v - V, w), \tag{9}$$

where $\mathbf{u}_{\boldsymbol{H}} = (u, v)$, $\mathbf{u} = (u, v, w)$, with u, v and w being the zonal, meridional, and vertical tidal velocities, respectively. SSH is denoted by η, the bottom depth by h, and the total water depth by $H = \eta + h$. The notation $\overline{(*)} = \int_{-h}^{\eta} * \, dz$ indicates the depth-integrated variable $*$ over the full water column.

The total density and hydrostatic pressure are partitioned into a constant reference state, background field, and perturbation due to wavy motion:

$$\rho = \rho_0 + \rho_b(z) + \rho'(x, y, z, t), \tag{10}$$

$$p = \rho_0 g(\eta - z) + g\int_z^{\eta} \rho_b \, dz + \int_z^{\eta} \rho' \, dz = p_0 + p_b + p'. \tag{11}$$

The depth-integrated energy conservation equation for barotropic and baroclinic tides (Llewellyn and Young 2002; Kang and Fringer, 2012; Tanaka, 2023) is

$$\frac{\partial \overline{E_{bt}} + \overline{E_{bc}}}{\partial t} + \nabla_H \cdot (\overline{\mathbf{F}_{\boldsymbol{bt}}} + \overline{\mathbf{F}_{\boldsymbol{bc}}}) = -D. \tag{12}$$

On the left-hand side of Eq. (12), the barotropic ($\overline{E_{bt}}$) and baroclinic ($\overline{E_{bc}}$) tidal energies are partitioned into kinetic components ($\overline{E_{Kbt}}$ and $\overline{E_{Kbc}}$), corresponding to Barotropic Kinetic Energy (BTKE) and Baroclinic Kinetic Energy (BCKE) and potential components $\overline{E_{Pbt}}$ and $\overline{APE}$, corresponding to Barotropic Potential Energy (BTPE) and Available Potential Energy (APE):

$$\overline{E_{bt}} = \overline{E_{Kbt}} + \overline{E_{Pbt}} = \frac{1}{2}\rho_0 H(U^2 + V^2) + \frac{1}{2}\rho_0 g\eta^2, \tag{13}$$

$$\overline{E_{bc}} = \overline{E_{Kbc}} + \overline{APE} = \frac{1}{2}\rho_0\overline{(u'^2 + v'^2 + w^2)} + \frac{1}{2}\rho_0\overline{N^{-2}b^2}, \tag{14}$$

where b is the buoyancy of the tidal disturbance and N the buoyancy frequency.

Energy fluxes of the barotropic and baroclinic tides are denoted as $\mathbf{F}_{\boldsymbol{bt}}$ and $\mathbf{F}_{\boldsymbol{bc}}$, respectively, and are partitioned into the advective and pressure work components:

$$\mathbf{F}_{bt} = \overline{\mathbf{U}E_{Kbt}} + \mathbf{U}H\rho_0 g\eta, \tag{15}$$

$$\mathbf{F}_{bc} = (\overline{\mathbf{u}_{\boldsymbol{H}}\mathrm{APE}} + \overline{\mathbf{u}_{\boldsymbol{H}}E_K} - \overline{\mathbf{U}E_{Kbt}}) + \rho_0 p'\mathbf{u}'. \tag{16}$$

The energy conversion rate from barotropic to baroclinic tides is calculated using the formula proposed by Kang and Fringer (2012). This rate is further partitioned into contributions from surface and topographic modes.

$$C = \overline{\rho' g W_S} + \overline{\rho' g W_T}, \tag{17}$$

$$W_S = -\nabla_H \cdot (h\mathbf{U}_{\boldsymbol{S}}) - z\nabla_H \cdot \mathbf{U}_{\boldsymbol{S}}, \tag{18}$$

$$W_T = -\nabla_H \cdot (h\mathbf{U}_{\boldsymbol{T}}) - z\nabla_H \cdot \mathbf{U}_{\boldsymbol{T}}. \tag{19}$$

On the right-hand side of Equation (12), *D* denotes the tidal dissipation term, which is treated as a residual in the calculation.

3 Results

3.1 General characteristics of diurnal and semi-diurnal tides

Tidal constituents within the same species exhibit similar fundamental wave patterns despite differences in amplitude, as their solutions to the governing hydrodynamic equations depend primarily on frequency (Roos et al., 2022). For simplicity, we select two representative tidal constituents, M_2 and K_1, to illustrate the general characteristics of diurnal and semi-diurnal tides, respectively.

The cotidal charts (Figs. 4a and 4b) show remarkable differences in the amplitude and propagation patterns between the M_2 and K_1 tidal waves. High tidal amplitudes are concentrated in two distinct regions: the continental slope, which is dominated by K_1, and the south-eastern ice shelf grounding zone, where both K_1 and M_2 are prominent. This distribution aligns with that reported by Robertson (2005). The K_1 tidal wave propagates from east to west, undergoing a reduction of phase speed as it passes over the slope. Notably, three distinct tidal amplitude peaks are found along the continental slope. This feature is evident across all diurnal constituents (Fig. 4c). The M_2 constituent propagates anticyclonically across the Ross Sea, forming an amphidromic point beneath the ice shelf (Robertson et al., 2003). This feature arises from destructive interference of semidiurnal Kelvin waves, which occurs because the Ross Sea coastline length is comparable to the tidal wavelength (MacAyeal, 1984b). Unlike diurnal constituents, the M_2 and other semi-diurnal constituents have no significant amplitude peaks along the slope (Fig. 4c).

In parallel to the tidal elevation patterns, the diurnal and semi-diurnal tides show pronounced differences in the barotropic tidal current fields. Over the continental slope, the K_1 constituent exhibits a complex flow regime with pronounced variations in both the magnitude and direction (Fig. 5b). In agreement with Robertson et al. (2003), the M_2 tidal flow is generally weak throughout the Ross Sea (Fig. 5a), except in the vicinity of the south-eastern ice shelf grounding zone, where current speeds exceed 0.1 m/s. The mean amplitudes of tidal cross-slope velocities shown in Figs. 5c and 5d suggest that the strength of both the semi-diurnal and diurnal currents is related to the bottom topography. For diurnal tides, significant velocities form a banded structure along the slope, spanning the entire water column with bottom intensification and reaching up to 20 cm/s. The semi-diurnal tidal currents are also bottom-intensified as well, though their speeds are much weaker (~ 5 cm/s). These patterns are linked to the eddy-like structures and bottom-trapped waves described in the following Sect. 3.2 and 3.3. In addition, a weak surface-intensified feature is found in Fig. 5d, which is likely induced by near-inertial winds (Brearley et al., 2017), as the local near-inertial frequency (~0.08 cph) is close to the semi-diurnal tidal frequency.

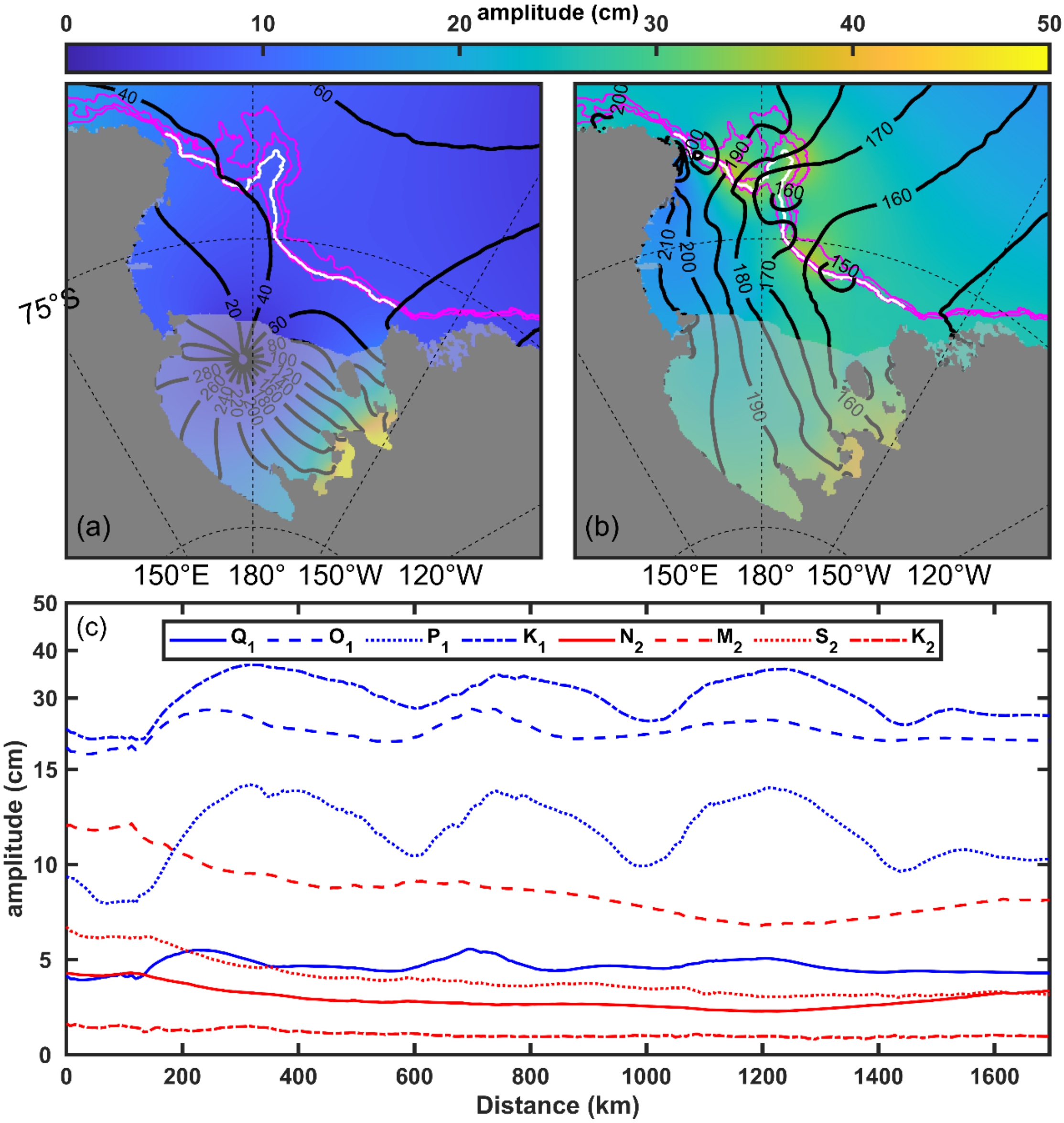

Figure 4. The cotidal charts of (a) M$_2$ and (b) K$_1$ tidal constituents from the model simulation. The co-phase lines are shown as black lines. The 500, 1000, and 2000-m isobaths (magenta) and the 700-m isobath (white) are shown along the continental slope. (c) The amplitude of individual constituents along the 700-m isobath.

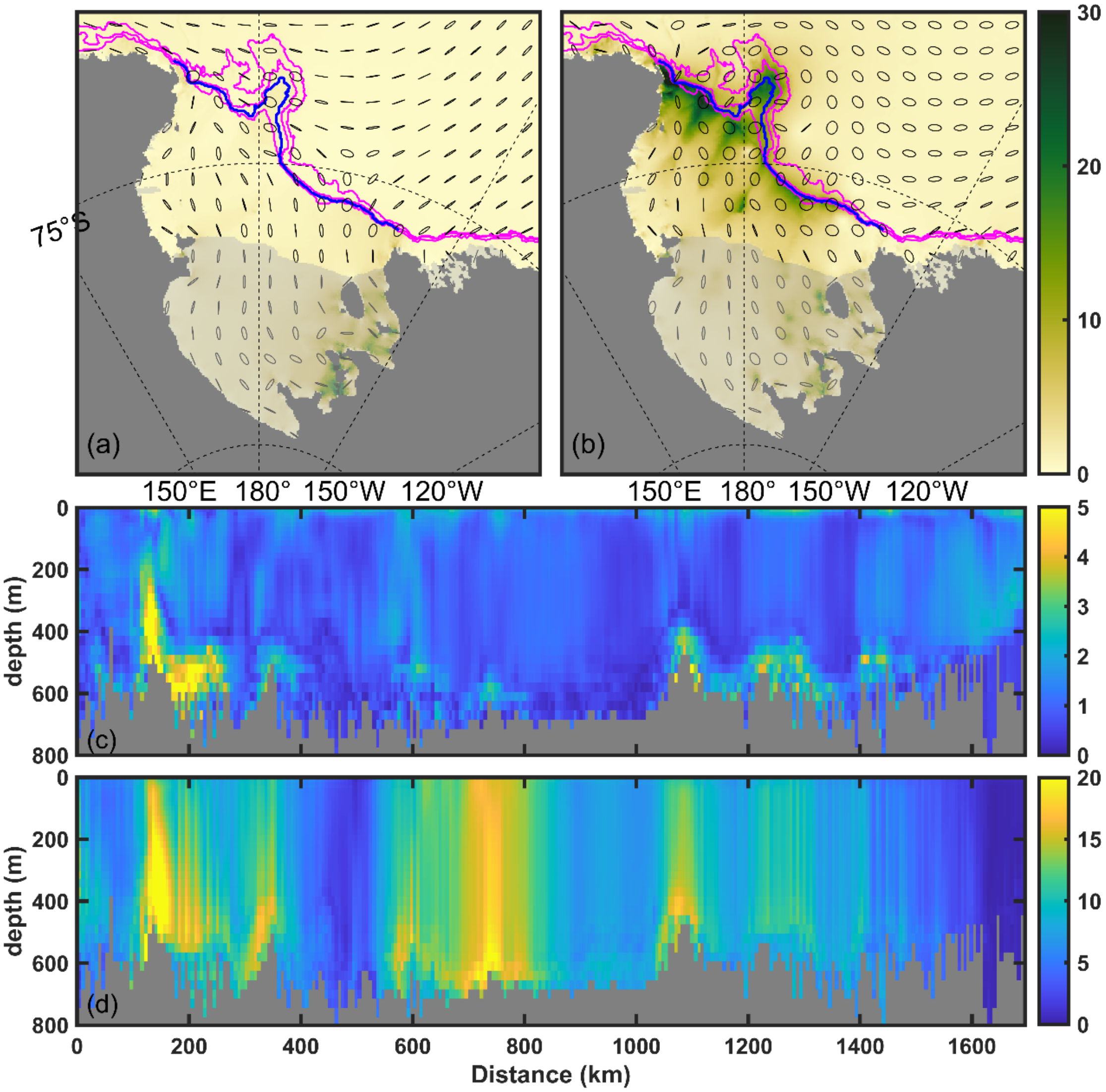

240

Figure 5. (a, b) Tidal ellipses for M$_2$ and K$_1$. Ellipse major axes are normalized; color shading shows actual speed (cm/s). The 500, 1000, and 2000-m isobaths (magenta) and the 700-m isobath (blue) are shown along the continental slope. (c, d) Vertical section of the mean amplitude of cross-slope tidal flow speed (cm/s) for the semidiurnal and diurnal constituents along the 700 m isobath.

3.2 Eddy-like structures in the topographic mode

245 As described in sect. 2.4, the barotropic tidal flow has been decomposed into the surface and topographic modes so as to elucidate how topography governs the flow structure. The decomposed topographic mode of diurnal tides, shown in Figs. 6a and 6b, exhibits three eddy-like structures over the continental, marked by distinct SSH anomalies. The direction of the flow, as well as the sign of the SSH anomalies, reverses between flood and ebb tides, indicating a direct dynamical coupling between them. However, according to the assumption of the decomposition framework, the topographic mode itself is nondivergent,

and the SSH anomalies are only related to the surface mode. Given the conservation of water mass, the tide-induced change in sea level Δη over any period can be written as a function of the divergence of the tide-induced volume transport:

$$\Delta\eta = \int \nabla \cdot (H\mathbf{u}_S)\, dt. \tag{20}$$

Integration over the flood and ebb tidal periods reveals that the pattern of surface-mode transport divergence (Figs. 6c and 6d) closely matches the SSH pattern (Figs. 6a and 6b). This agreement confirms that the SSH anomalies arise from the surface mode. During the flood period, as the surface-mode tidal flow encounters the continental slope, it adjusts to the topography and generates three SSH maxima through convergence. In contrast, during the ebb period, the flow diverges over the slope, producing three SSH minima that mirror the flood-time pattern. Critically, for diurnal tides, the SSH anomalies can persist for 6 hours, which is longer than the geostrophic adjustment timescale (1/f ≈ 2 hours), thus allowing for the formation of eddy-like flows seen in the topographic mode. For semi-diurnal tides, the tidal flow is much weaker, and its surface mode shows negligible divergence (Figs. 7c and 7d). This leads to no significant SSH anomalies over the slope (Figs. 7a and 7b). Additionally, the semi-diurnal flood/ebb period is likely too short for geostrophic adjustment to establish organized currents. Consequently, no eddy-like features appear in the topographic mode of semi-diurnal tides.

Since the topographic mode dominates the tidal flow over the continental slope, it is instructive to quantify its role in cross-slope transport. The cross-slope volume (VT) and heat (HT) transport through the 700-m isobath are calculated as

$$VT = \int_0^L \int_{-H}^0 \mathbf{u} \cdot \frac{\nabla h}{|\nabla h|}\, dz dl, \tag{21}$$

$$HT = \int_0^L \int_{-H}^0 \rho c_p (T - T_f) \mathbf{u} \cdot \frac{\nabla \mathrm{h}}{|\nabla \mathrm{h}|}\, dz dl, \tag{22}$$

where **u** can be decomposed into the surface- and topographic-mode tidal velocity vectors, $c_p = 3994\ \mathrm{J/(kg \cdot {}^\circ C)}$ is the specific heat capacity, T is the potential temperature, and $T_f = -1.9\ {}^\circ\mathrm{C}$ is the freezing point of seawater. Positive (negative) values of VT or HT indicate onshore (offshore) transport.

As shown in Figs. 8a-8c, the topographic mode is the primary driver of local instantaneous transport, surpassing the surface mode in regulating shelf-basin exchange. Nevertheless, its integrated transport along the entire 700-m isobath is nearly zero, indicating that it does not contribute to a net cross-slope volume flux. Time averaging (Figure 8g) further illustrates that the offshore volume transport by the topographic mode offsets the onshore transport by the surface model so that the volume is conserved.

For cross-slope heat transport (Figs. 8d-8f), the topographic-mode tides are even more influential, dictating local heat transport while also accounting for the majority of the instantaneous onshore flux. This is striking because, despite the absence of net volume transport, the tidal heat flux across the 700-m isobath can reach 12 TW, with most of which being attributable to the topographic mode (Fig. 8h).

https://doi.org/10.5194/egusphere-2026-2988
Preprint. Discussion started: 5 June 2026

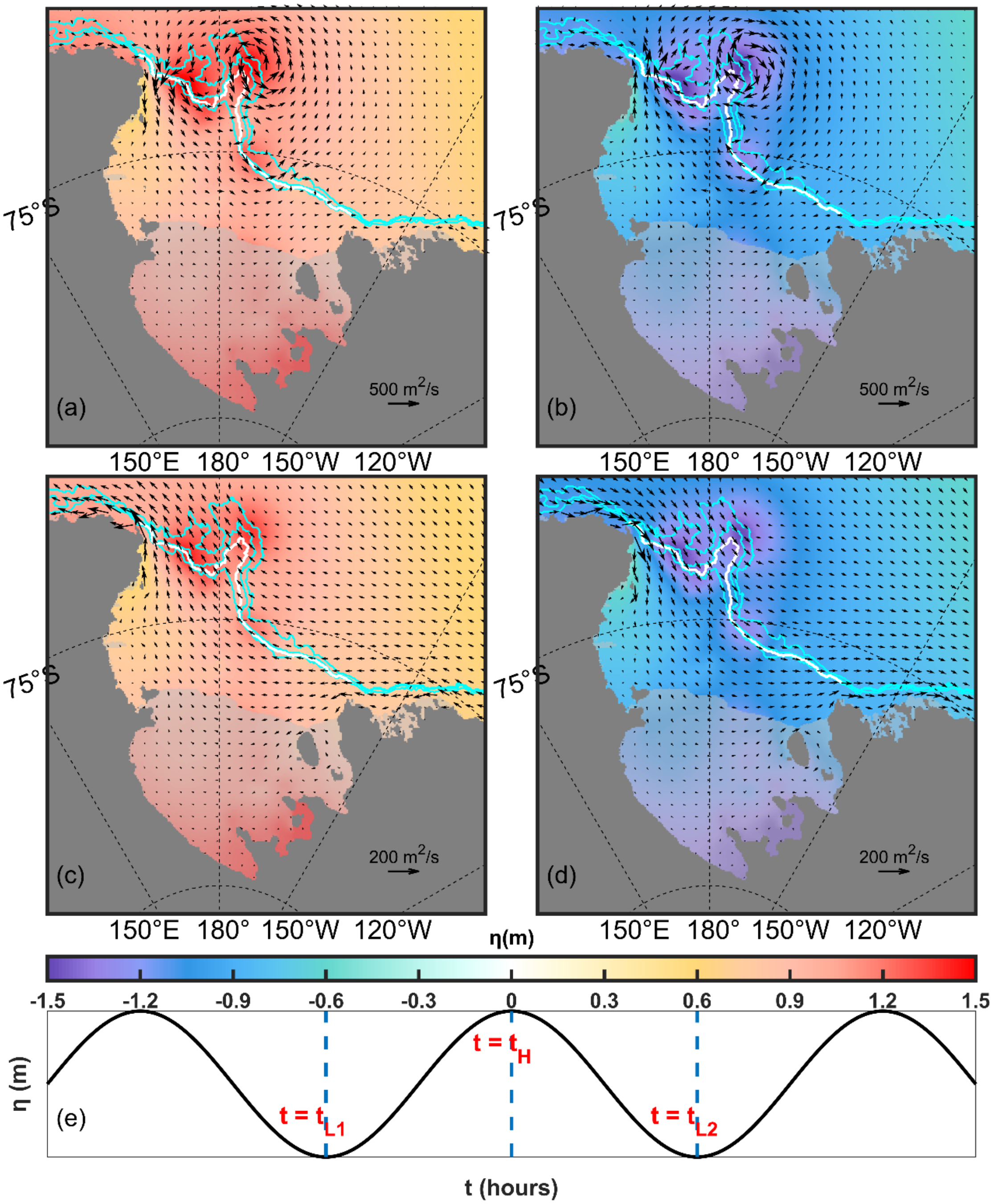

Figure 6. (a) Tide-induced sea level change (color shading) during flood period (from t_{L_1} to t_H), overlain by volume transport vectors of the topographic mode at t_H. (b) Tide-induced sea level change (color shading) during ebb period (from t_H to t_{L_2}), overlain by volume transport vectors of the topographic mode at t_{L_2}. (c, d) Corresponding volume divergence due to the surface mode (color shading) during flood and ebb periods, overlain by volume transport vectors of the surface mode at t_H and t_{L_2}, respectively. The 500, 1000, and 2000-m isobaths (cyan) and the 700-m isobath (white) are shown along the continental slope. (e) Schematic for illustrating the flood and ebb periods for integration.

290

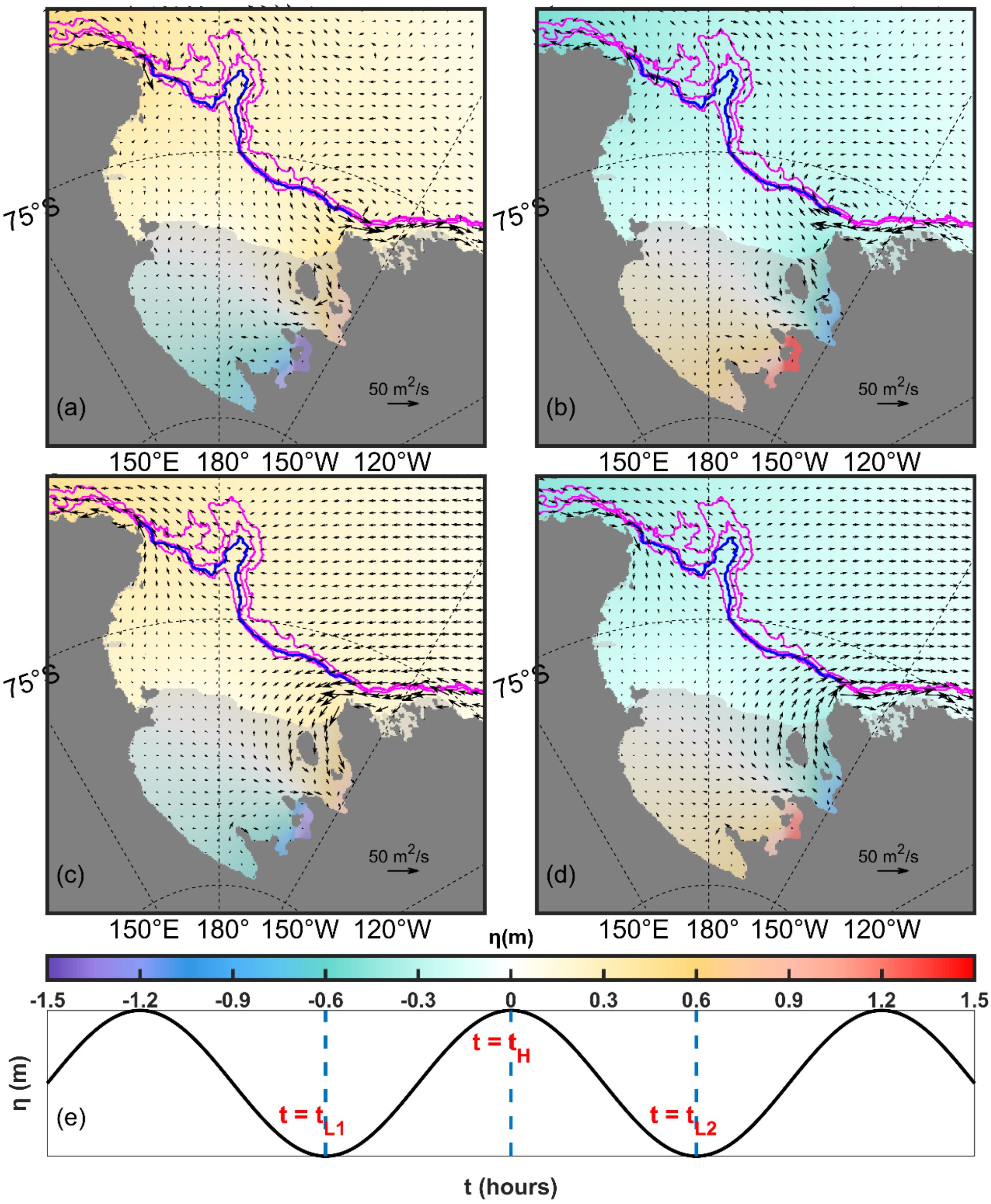

Figure 7. Same as Fig.6, but for semi-diurnal tides.

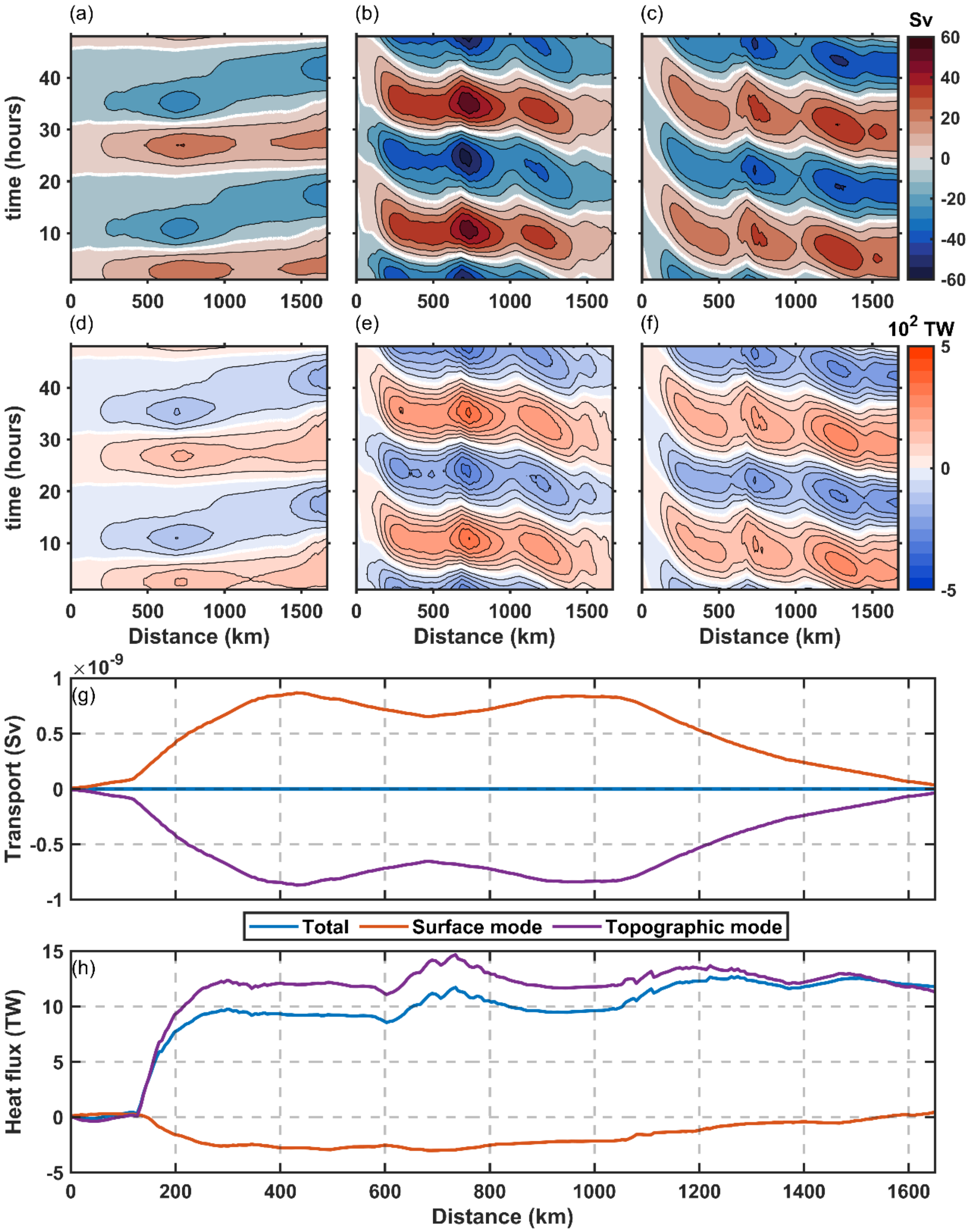

Figure 8. (a-c) Cross-slope volume transport integrated along the 700-m isobath as a function of time for (a) the surface mode, (b) the topographic mode, and (c) their sum. (d-f) The corresponding heat transport. (g, h) The temporal averages of the volume and heat transport, respectively. Positive (negative) values indicate onshore (offshore) transport.

3.3 Bottom-Trapped Waves and Energetics

Since most of the Ross Sea lies poleward of the semi-diurnal critical latitude (~74.5°S) and its tidal regime is diurnal-dominated, internal tides generated by the barotropic tide-topography interaction are bottom-trapped, which can result in an intensification of the near-bottom flow and shear (D'Asaro and Morison, 1992). This expectation is confirmed by our model results. As shown in Figs. 9a and 9b, both the baroclinic kinetic energy density and squared vertical shear are intensified within the bottom tens of meters, implying the presence of bottom-trapped waves. The vertical extent of these waves varies with the tidal cycle, increasing significantly during spring tide and shrinking or even vanishing during neap tide. Note that the term "bottom-trapped" refers to an energy maximum near the bottom, not the absence of baroclinic flow above it. These waves form through constructive interference of individual modes (Falahat and Nycander, 2015).

Since water depth varies spatially across the Ross Sea, a fixed critical depth cannot accurately describe bottom-intensified waves. To map their distribution, we define a non-dimensional relative depth (RD):

$$RD = \frac{H_m}{H}, \tag{23}$$

where H_m denotes the depth at which the kinetic energy density reaches its maximum. The RD ranges from 0 to 1, and a value close to 1 indicates the presence of bottom intensification. To ensure the identified bottom-trapped signals are significant, we applied RD calculation only when the barotropic kinetic energy density exceeded 1.2975 J/m^3 (corresponding to a velocity of 5 cm/s) and the maximum kinetic energy density was greater than 1.2 times the barotropic value.

The spatial pattern of RD in Fig. 9c reveals significant bottom intensification over the continental slope and topographic features such as banks and troughs, while it is minimal under the ice shelf and over the slope east of Houtz Bank (HoB). The bottom-trapped waves cause vertical displacement of bottom water particles, which peaks north of DT at meter-scale amplitudes (Fig. 9d). This is much smaller than the hundred-meter amplitudes of freely propagating internal tides (e.g., in the Bay of Biscay, see Pairaud et al., 2010), highlighting the bottom-trapped nature of Ross Sea internal tides.

The energy conversion between the surface and topographic tidal modes is shown in Fig. 10a. A positive value denotes energy transfer from the surface to the topographic mode, and vice versa. As expected, the conversion is concentrated over topographic features, with the magnitude of 1 W/m², much greater than the BT-BC energy conversion rate (Fig. 10b). The pattern reveals large alternating positive and negative patches, which are associated with the eddy-like structures in the topographic mode (Fig. 6). The conversion rate varies in sign along the slope because the eddies' velocities are alternately aligned with or against the surface mode. In addition, smaller-scale patches are found along the coast, which are likely related to coastal trapped waves.

Energy conversion from barotropic to baroclinic tides in the Ross Sea mainly occurs over the slope and peaks near the mouth of DT (Fig. 10b), with a rate of approximately 10^{-2} W/m². While this value is considerably lower than that in other oceans (Kang and Fringer, 2012; Müller, 2013; Han and Eden, 2019), it is of the same order as the estimates derived using the method of Falahat and Nycander (2015), wherein the rate is obtained by dividing the baroclinic energy density (Figs. 11c and 11d) by a decay time of 2–3 days. The energy conversion from barotropic to baroclinic tides is separated into contributions from the surface (Fig. 10c) and topographic modes (Fig. 10d), respectively. It is evident that the topographic mode dominates the conversion to baroclinic tides in most of the region. Notably, the surface mode appears to extract energy from the baroclinic tides, especially near the mouth of DT (negative values in Fig. 10c). This implies a cyclic energy pathway there: from the surface to the topographic mode, then to the baroclinic tides, and back to the surface mode.

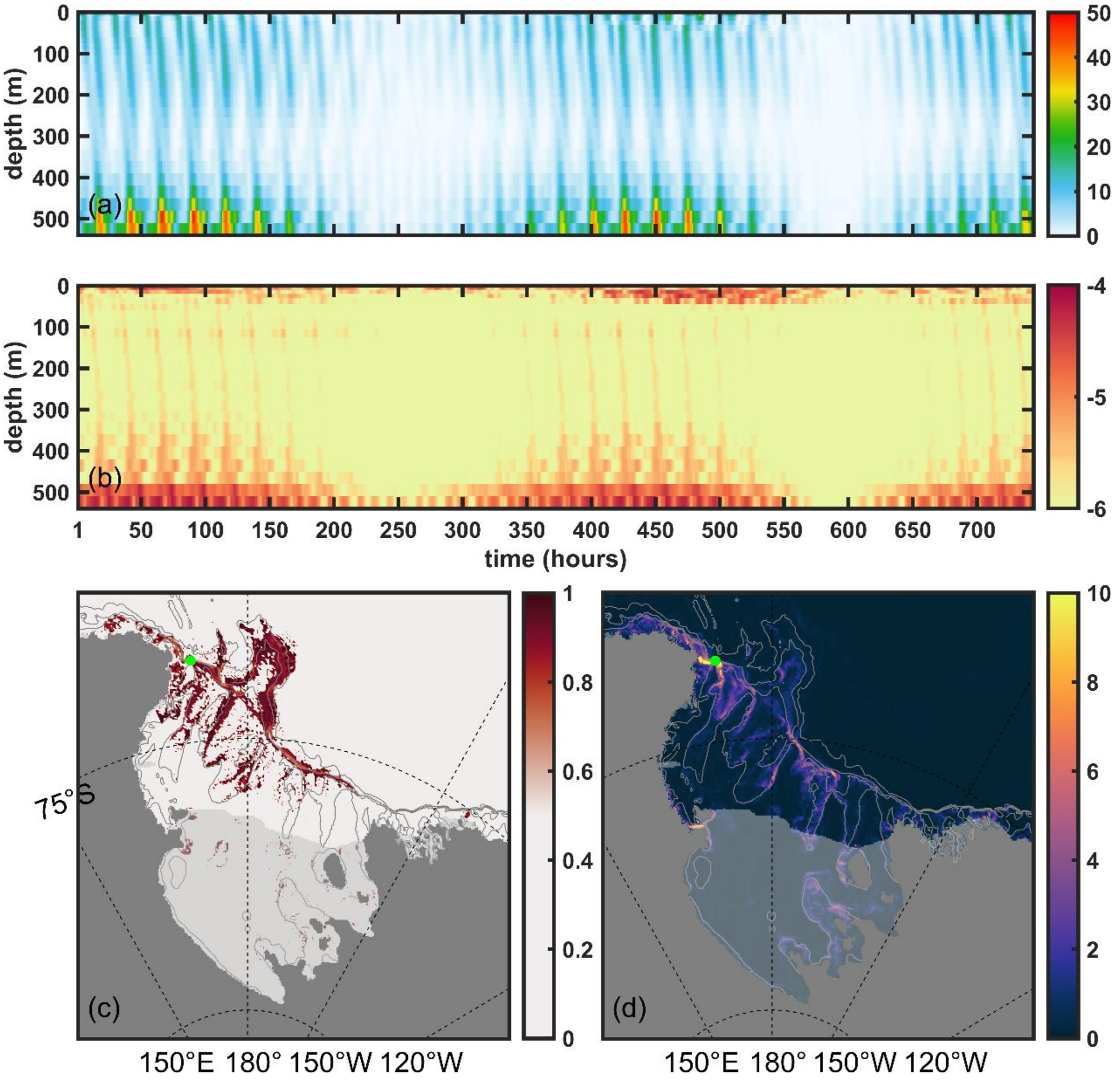

Figure 9. Time-depth plot of the (a) baroclinic kinetic energy density (J/m^3) and (b) common logarithm of square of the vertical shear of tidal velocity $\log_{10}\left(\frac{\partial u}{\partial z}\right)^2+\left(\frac{\partial v}{\partial z}\right)^2$ (s^{-2}) at the point marked by green dots in panels (c, d) (close to mooring cc1) from the model simulation. (c) Map of the Relative Depth (RD). (d) Map of the maximum vertical displacement (m) of time-averaged density at the bottom of each water column. Bathymetry contours are spaced at 500, 1000, and 2000 m.

The energy conversion between the surface and topographic tidal modes is shown in Fig. 10a. A positive value denotes energy transfer from the surface to the topographic mode, and vice versa. As expected, the conversion is concentrated over topographic features, with the magnitude of 1 W/m², much greater than the BT-BC energy conversion rate (Fig. 10b). The pattern reveals large alternating positive and negative patches, which are associated with the eddy-like structures in the topographic mode (Fig. 6). The conversion rate varies in sign along the slope because the eddies' velocities are alternately aligned with or against the surface mode. In addition, smaller-scale patches are found along the coast, which are likely related to coastal trapped waves. Energy conversion from barotropic to baroclinic tides in the Ross Sea mainly occurs over the slope and peaks near the mouth of DT (Fig. 10b), with a rate of approximately 10^{-2} W/m². This order of magnitude is consistent with the estimates of Müller (2013), who applied a global model and used a methodology similar to ours. It also agrees with the estimates derived from the method of Falahat and Nycander (2015), in which the rate is obtained by dividing the baroclinic energy density (Figs. 11b and 11d) by a decay time of 2–3 days. However, the model of Müller (2013) produces higher conversion rate near the Iselin Bank (IB) than our model. This discrepancy is likely due to the difference in horizontal and vertical resolution (Niwa and Hibiya, 2011). The BT-BC conversion rate in the Ross Sea is considerably lower than that in other oceans (Kang and Fringer, 2012; Han and Eden, 2019), indicating weaker internal tide energy. The BT-BC conversion rate is separated into contributions from the surface (Fig. 10c) and topographic modes (Fig. 10d), respectively. It is evident that the topographic mode dominates the conversion to baroclinic tides in most of the region. Notably, the surface mode appears to extract energy from the baroclinic tides (negative values in Fig. 10c). This implies a cyclic energy pathway: from the surface to the topographic mode, then to the baroclinic tides, and back to the surface mode.

Figure 11 presents the depth-integrated, period-averaged tidal energy densities in the Ross Sea. The total baroclinic energy densities (Figs. 11b and 11d) are of the same order as the theoretical estimates of Falahat and Nycander (2015), which are based on barotropic tidal velocities and topographic gradients. Overall, BTKE exceeds BCKE by an order of magnitude, which is supported by the low energy BT-BC conversion rate shown in Fig. 10b. Furthermore, the total tidal potential energy is itself an order of magnitude smaller than the kinetic energy, and within it, APE is an order of magnitude smaller than BTPE. The enhancement of BTKE along the slope is modulated by the topographic mode (Fig. 6c). Specifically, it is strongest where three eddy-like structures are present (Fig. 11a). Meanwhile, the enhancement of BTPE over the slope is associated with the surface mode of the diurnal tide (Fig. 11c). The APE reaches its maximum over the DT, corresponding to the vertical displacement shown in Fig. 9d. Although BCKE is relatively small in the depth-integrated sense, it is significant near the seafloor because baroclinic tides in the Ross Sea are predominantly bottom-trapped waves. This confinement of energy to the bottom boundary layer may enhance the mixing.

The barotropic and baroclinic energy fluxes exhibit remarkable differences in both magnitude and spatial pattern. For clarity, only the high-tide snapshots are displayed in Figure 12. The complete figure set, covering time-average values, high-tide snapshots, and low-tide snapshots, is shown in Supplementary Figure S17. The barotropic tidal energy flux is dominated by the pressure work (Fig. 12a), with the advective component being two orders of magnitude smaller (Fig. 12b). Both barotropic components are significantly shaped by the topographic mode but respond differently to tidal phase. The simultaneous sign change of sea surface perturbation and tidal velocity causes the pressure-work-induced energy flux to maintain a consistent direction over the slope (Figs. 12a and S17c). The advective flux, however, reverses direction between flood and ebb (Figs.

https://doi.org/10.5194/egusphere-2026-2988
Preprint. Discussion started: 5 June 2026

12b and S17f). Consequently, the time-averaged energy flux from pressure work retains eddy-like patterns along the slope (Fig. S17a), whereas the advective component is largely cancelled out (Fig. S17d).

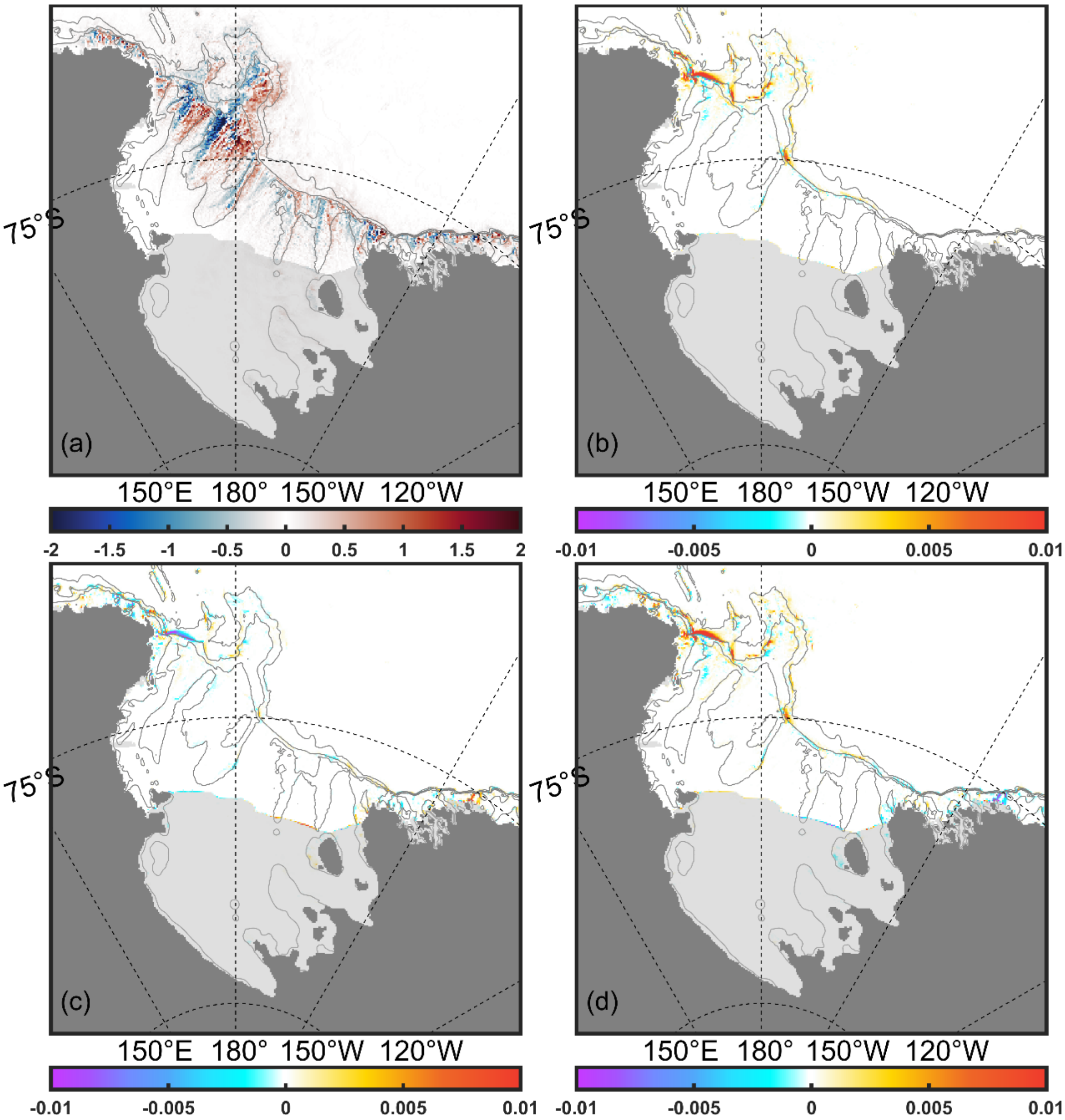

Figure 10. The rate of energy conversion (W/m^2) from (a) Surface mode to Topographic mode, (b) Barotropic (Surface + Topographic modes) tides to baroclinic tides, (c) Topographic mode to baroclinic tides, and (d) Surface mode to baroclinic tides. Bathymetry contours are spaced at 500, 1000, and 2000 m.

The baroclinic energy fluxes from pressure work and advection are comparable in magnitude, peaking around the DT and IB (Figs. 12c and 12d) in a pattern consistent with the BCKE distribution (Fig. 11b). Moreover, the magnitude is consistent with that reported by Müller (2013) in the Ross Sea. The pressure-work-induced baroclinic energy flux exhibits a disorganized directional pattern (Fig. 12c). This disorder arises because bottom-trapped internal waves differ fundamentally from free-propagating waves, which radiate internal tide energy in coherent beams. In contrast, the velocity and pressure structures of bottom-trapped waves are governed by the topographic gradients and the distance from the generation site (Falahat and Nycander, 2015). Consequently, the irregularity of the topography induces a complex interference pattern as waves generated at sites overlap, ultimately leading to this disordered state.

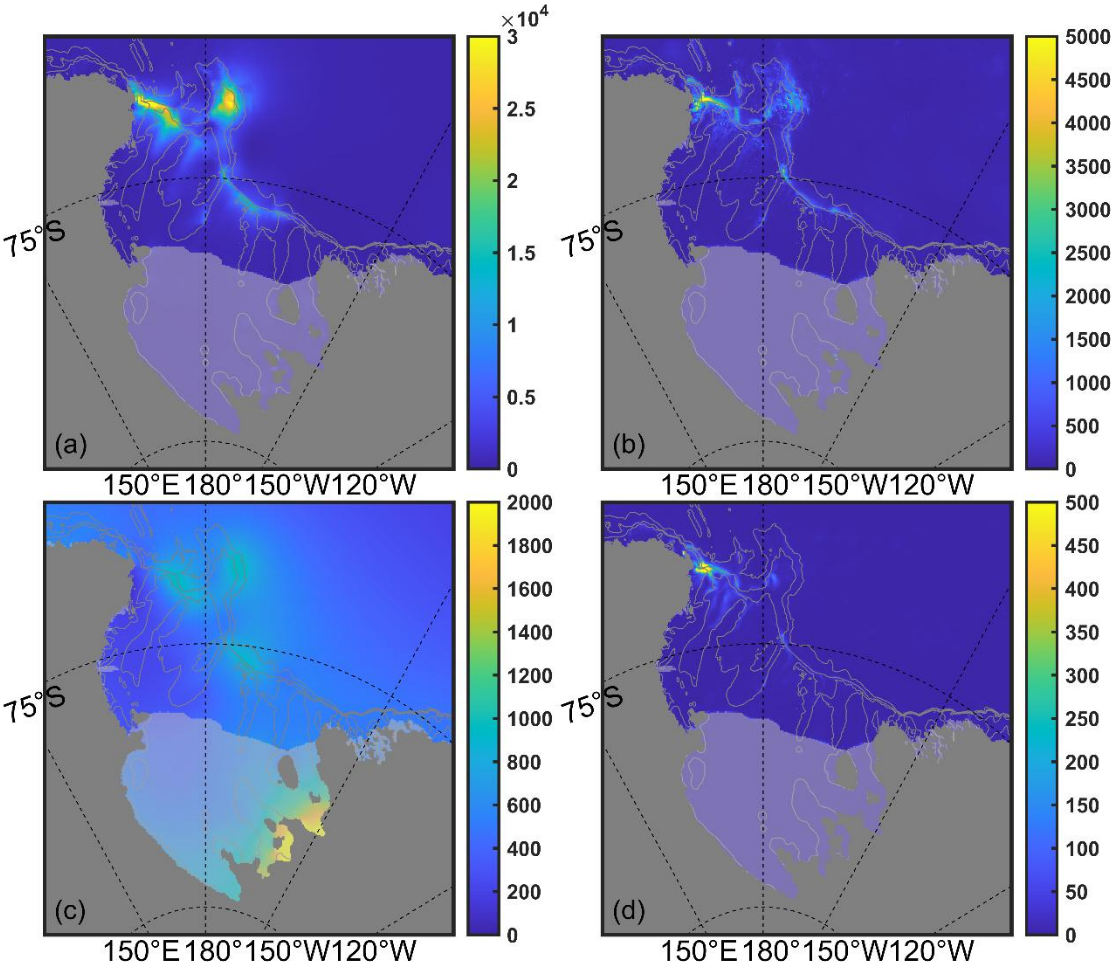

Figure 11. Spatial distribution of depth-integrated, period-averaged (a) barotropic kinetic energy density (J/m^2), (b) baroclinic kinetic energy density (J/m^2), (c) barotropic potential energy density (J/m^2), and (d) available potential energy density (J/m^2). Bathymetry contours are spaced at 500, 1000, and 2000 m.

Figure 13 shows that tidal energy dissipation is strongest along the continental slope, especially to the west near Cape Adare. The internal tide energy, though dissipated locally, is too weak to contribute significantly. Hence, the dissipation is overwhelmingly caused by barotropic tides. A dedicated calculation of the baroclinic dissipation was not performed, as the velocity enhancement due to internal tides in the Ross Sea is confined to a thin near-bottom layer ($\leq$50 m), which cannot be fully resolved due to the limitation of vertical resolution (the model's grid thickness is 30 m at the 500-m depth). The vertically integrated baroclinic energy flux is therefore overwhelmingly determined by, and highly sensitive to, the flow in the lowest few, partially filled grid cells. The complex geometry of these cells near the steep slope, combined with the C-grid's staggered variable layout, introduces significant numerical uncertainty.

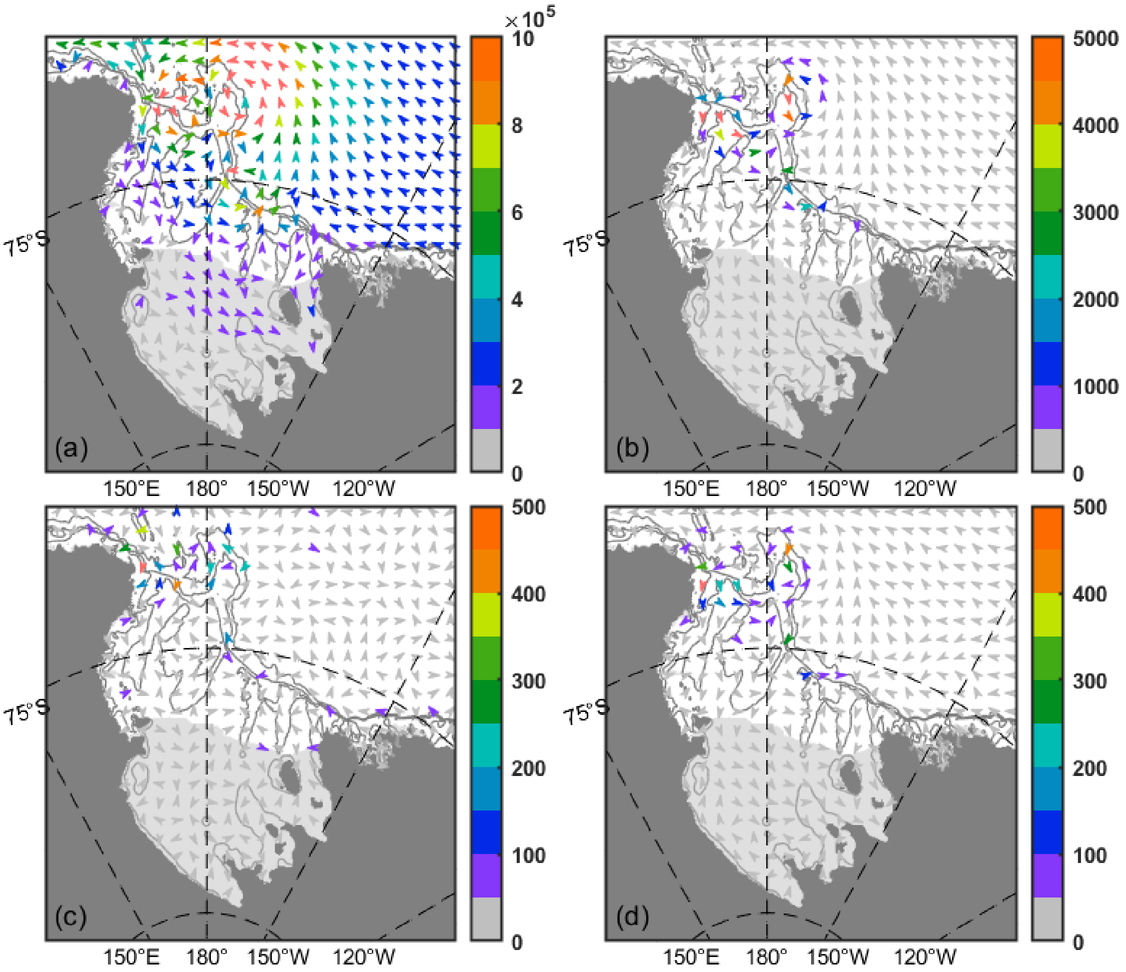

Figure 12. Depth-integrated energy flux (W/m) components (snapshots at high tide): (a) barotropic pressure work, (b) barotropic advective work, (c) baroclinic pressure work, and (d) baroclinic advective work. 405

https://doi.org/10.5194/egusphere-2026-2988
Preprint. Discussion started: 5 June 2026

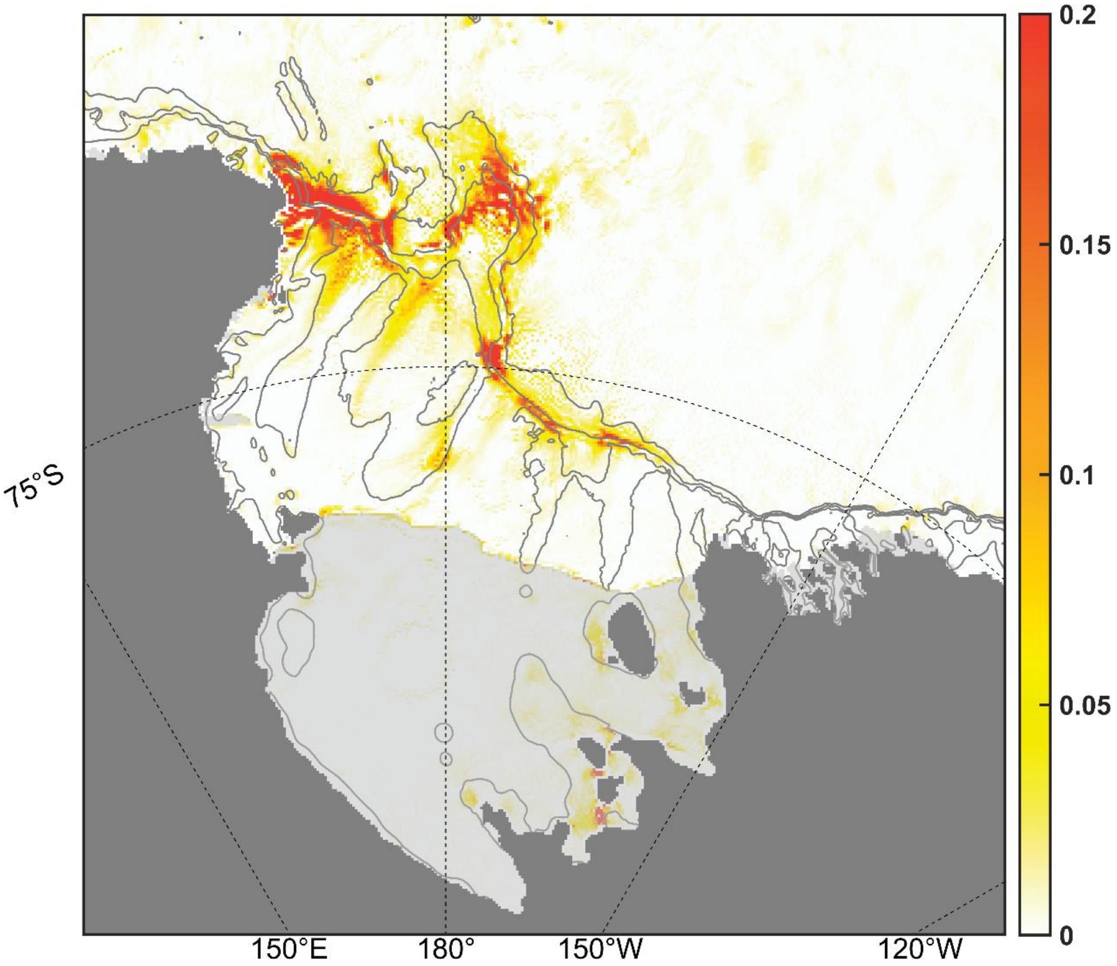

Figure 13. Map of the depth-integrated, period-averaged tidal dissipation rate (W/m^2). Bathymetry contours are spaced at 500, 1000, and 2000 m.

4 Summary and discussions

410 Using a three-dimensional high-resolution regional model, we investigated the characteristics of tides in the Ross Sea, with a focus on the eddy-like topographic mode and bottom-trapped waves through modal decomposition and energy budget analysis. The model shows good phase agreement with observations, although simulated amplitudes are slightly weaker. Our results confirm a spatial pattern consistent with earlier work: diurnal tides dominate the continental slope, while both diurnal and semi-diurnal constituents are prominent in the south-eastern grounding zone beneath the ice shelf, where the semi-diurnal tide establishes an amphidromic point system.

On the continental slope, diurnal and semi-diurnal tides differ in tidal amplitude and current structure. Diurnal constituents exhibit three distinct amplitude peaks, absent in semi-diurnal tides. Semi-diurnal currents show bottom intensification, whereas diurnal currents display a more complex pattern with bottom intensification plus full-water-column enhancement. Modal decomposition of the diurnal tides shows that convergence and divergence of the surface-mode flow generate three SSH extremes along the slope. These SSH anomalies persist long enough for geostrophic adjustment, giving rise to three eddy-like structures in the diurnal topographic mode. Semi-diurnal tides exhibit no such features because they are too weak to generate SSH extremes, and their period is too short for geostrophic adjustment to occur. The topographic mode governs local cross-slope volume and heat transport, with a time-averaged onshore heat flux of ~12 TW. Energy conversion between the surface and topographic modes reaches ~1 W m^{-2} along the slope.

Baroclinic tides in the Ross Sea, though an order of magnitude weaker in energy than barotropic tides, exist primarily as bottom-trapped waves over the slope, banks, and troughs. They drive several meters of vertical displacement and generate a near-bottom shear layer tens of meters thick. This layer expands during spring tides and nearly vanishes during neap tides. Energy budget analysis reveals that the barotropic-to-baroclinic conversion rate in the Ross Sea is only ~0.01 W m^{-2}, much weaker than values reported for other oceans (e.g. Kang and Fringer, 2012). Barotropic tidal energy flux is dominated by pressure work, with advection an order of magnitude smaller; its spatial patterns are strongly modulated by the topographic mode. In contrast, baroclinic energy fluxes from pressure work and advection are comparable, indicating significant nonlinearity within the internal tide field. These fluxes peak near Drygalski Trough and Iselin Bank. Strong tidal dissipation (~0.1 W m^{-2}) occurs along the slope, mainly attributed to barotropic tides, as internal tide energy is too weak to contribute appreciably to the total dissipation.

This study quantifies the heat transport associated with the topographic mode along the Ross Sea continental slope, providing a basis for further assessing tidal influences on ice shelf melting. This heat, delivered by topographically controlled tidal flows, has direct implications for basal melting rates, freshwater fluxes, and the stability of the ice shelf. Moreover, by modulating cross-slope exchange, these tidal processes influence the formation and transport of key water masses, including DSW and AABW, which ventilate the global abyssal ocean. The eddy-like structures and bottom-trapped waves we describe may also enhance mixing and heat redistribution along the slope, with potential feedbacks on sea ice formation, polynya dynamics, and the broader Antarctic climate system.

This study has some limitations. First, the small Rossby radius of deformation in the Ross Sea (~6 km) requires a model horizontal resolution finer than 1 km to fully resolve mesoscale eddies (Hallberg, 2013). Owing to the poor representation of mesoscale eddies, our model may have overestimated tidal heat transport across the continental slope—a transport that should be partly contributed by eddies. Second, baroclinic tidal energy in the Ross Sea is dominated by bottom-trapped waves, but the vertical resolution of our model is insufficient to fully resolve the vertical structure of these waves over the continental slope. This limitation likely leads to an underestimation of baroclinic energy and, consequently, baroclinic dissipation. A model with higher horizontal and vertical resolution is needed to obtain a complete representation of tidal energetics in the Ross Sea.

Data availability

The ERA5 product is available from the Copernicus Climate Data Store at https://doi.org/10.24381/cds.adbb2d47 (Hersbach et al., 2023). The RTopo-2 data is available through the PANGAEA Data Publisher for Earth and Environmental Science at https://doi.pangaea.de/10.1594/PANGAEA.856844 (Schaffer and Timmermann, 2016). SOSE data is obtained from the Scripps Institution of Oceanography (https://sose.ucsd.edu/sose_stateestimation_data_05to10.html). Sea ice data from the National Snow and Ice Data Center is available at https://doi.org/10.7265/N5K072F8 (Fetterer et al., 2017). The AnSlope data is collected by Antarctic Slope program (https://ocp.ldeo.columbia.edu/res/div/ocp/projects/anslope/Data.html). The CATS2008 data is obtained from the U.S. Antarctic Program Data Center at https://www.esr.org/data-products/polar-tide-models/list-of-polar-tide-models/cats2008.

Author contributions

Yue Xia served as the primary author, leading the investigation, performing the experiments, and preparing the original draft, including visualization. Hengling Leng (Corresponding author) contributed to conceptualization, methodology, supervision, funding acquisition, and review/editing. Zhaomin Wang, Chengyan Liu contributed to funding acquisition and review/editing, Liangjun Yan contributed to resources and review/editing, Xianxian Han contributed to methodology and review/editing. Craig Stevens and Dake Chen contributed to review/editing.

Competing interests

The authors declare no conflicts of interest relevant to this study.

Disclaimer

Financial support

This research was supported by the National Key Research and Development Project of China (Grant 2024YFF0506603), the China National Natural Science Foundation (NSFC) Project (42576020 and 42306025), the Independent Research Foundation of Southern Marine Science and Engineering Guangdong Laboratory (Zhuhai) (SML2023SP201 and SML2021SP306), and the Guangdong Basic and Applied Basic Research Foundation, China (2024A1515012717 and 2026A1515012241).

References

Brearley, J. A., Meredith, M. P., Garabato, A. C. N., Venables, H. J., Inall, M.E.: Controls on turbulent mixing on the West Antarctic Peninsula shelf. Deep-Sea Res. Pt. II., 139, 18-30, https://doi.org/10.1016/j.dsr2.2017.02.011, 2017.

Bell, T. H.: Lee waves in stratified flows with simple harmonic time dependence. J. Fluid Mech., 67, 705–722, https://doi.org/10.1017/S0022112075000560, 1975.

Brunt, K. M., King, M. A., Fricker, H. A., and MacAyeal, D. R.: Flow of the Ross Ice Shelf, Antarctica, is modulated by the ocean tide. J. Glaciol., 56, 157–161, https://doi.org/10.3189/002214310791190875, 2010.

Castagno, P., Falco, P., Dinniman, M. S., Spezie, G., and Budillon, G.: Temporal variability of the Circumpolar Deep Water inflow onto the Ross Sea continental shelf. J. Mar. Syst., 166, 37–49, https://doi.org/10.1016/j.jmarsys.2016.05.006, 2017.

Chen, C., and Beardsley, R. C.: A Numerical Study of Stratified Tidal Rectification over Finite-Amplitude Banks. Part I: Symmetric Banks. J. Phys. Oceanogr., 25, 2090-2110, https://doi.org/10.1175/1520-0485(1995)025<2090:ANSOST>2.0.CO;2, 1995.

Darwin, G. H.: On the Antarctic Tidal Observations of the 'Discovery.', in: The Scientific Papers of Sir George Darwin (Original version published 1907): Oceanic Tides and Lunar Disturbance of Gravity, Cambridge University Press, Cambridge, 372–388, https://doi.org/10.1017/CBO9780511703461.014, 2009.

D'Asaro, E. A.; Morison, J. H.: Internal waves and mixing in the Arctic Ocean. Deep-Sea Res. Pt. A, 39, S459–S484, https://doi.org/10.1016/S0198-0149(06)80016-6, 1992.

Determann, J., and Gerdes, R.: Melting and freezing beneath ice shelves: implications from a three-dimensional ocean-circulation model. Ann. Glaciol., 20, 413–419, https://doi:10.3189/1994AoG20-1-413-419, 1994.

Doake, C. S. M., Corr, H. F. J., Nicholls, K. W., Gaffikin, A., Jenkins, A., Bertiger, W. I., and King, M. A.: Tide-induced lateral movement of Brunt Ice Shelf, Antarctica. Geophys. Res. Lett., 29, https://doi.org/10.1029/2001GL014606, 2002.

Falahat, S., and Nycander, J.: On the Generation of Bottom - Trapped Internal Tides. J. Phys. Oceanogr., 45, 526-545, https://doi.org/10.1175/JPO-D-14-0081.1, 2015.

Fetterer, F., Knowles, K., Meier, W. N., Savoie, M., and Windnagel, A. K.: Sea ice index, version 3. NSIDC: National Snow and Ice Data Center [data set]. updated daily. https://doi.org/10.7265/N5K072F8, 2017.

Flexas, M.M., Schodlok, M.P., Padman, L., Menemenlis, D., and Orsi, A.H.: Role of tides on the formation of the Antarctic Slope Front at the Weddell-Scotia Confluence. J. Geophys. Res.-Oceans, 120, 3658-3680, https://doi.org/10.1002/2014JC010372, 2015.

Fricker, H. A., and Padman, L.: Ice shelf grounding zone structure from ICESat laser altimetry, Geophys. Res. Lett., 33, L15502, https://doi.org/10.1029/2006GL026907, 2006.

Garreau, P., and Maze, R.: Tidal Rectification and Mass Transport over a Shelf Break: A Barotropic Frictionless Model. J. Phys. Oceanogr., 22, 719-731, https://doi.org/10.1175/1520-0485(1992)022<0719:TRAMTO>2.0.CO;2, 1992.

Gilmour, A. E., Macdonald, W. J. P., and van der Hoeven, F. G.: Winter measurements of sea currents in McMurdo Sound. N. Z. J. Geol. Geophys., 5, 778–789, https://doi.org/10.1080/00288306.1962.10417637, 1962.

Gordon, A. L., E. Zambianchi, A. Orsi, M. Visbeck, C. F. Giulivi, T. Whitworth III, and G. Spezie.: Energetic plumes over the western Ross Sea continental slope, Geophys. Res. Lett., 31, L21302, https://doi.org/10.1029/2004GL020785, 2004.

Guan, X., Ou, H.-W., and Chen, D.: Tidal effect on the dense water discharge, Part 2: A numerical study. Deep-Sea Res. Pt. II, 56, 884–894, https://doi.org/10.1016/j.dsr2.2008.10.028, 2009.

Hallberg, R.: Using a resolution function to regulate parameterizations of oceanic mesoscale eddy effects. Ocean Modell., 72, 92–103, https://doi.org/10.1016/j.ocemod.2013.08.007, 2013.

Han, B., Eden, C.: The energetics of internal tides at the Luzon Ridge. Ocean Dyn., 69, 1009–1022, https://doi.org/10.1007/s10236-019-01297-9, 2019.

Han, X., Stewart, A. L., Chen, D., Janout, M., Liu, X., Wang, Z., and Gordon, A. L.: Circum-Antarctic bottom water formation mediated by tides and topographic waves. Nat. Commun., 15(1), 2049, https://doi.org/10.1038/s41467-024-46086-1, 2024.

Han, X., Stewart, A. L., Chen, D., Liu, X., and Lian, T.: Controls of Topographic Rossby Wave Properties and Downslope Transport in Dense Overflows. J. Phys. Oceanogr., 53, 1805-1820, https://doi.org/10.1175/JPO-D-22-0237.1, 2023.

Hersbach, H., Bell, B., Berrisford, P., Biavati, G., Horányi, A., Muñoz Sabater, J., Nicolas, J., Peubey, C., Radu, R., Rozum, I., Schepers, D., Simmons, A., Soci, C., Dee, D., and Thépaut, J.-N.: ERA5 hourly data on single levels from 1940 to present. Copernicus Climate Change Service (C3S) Climate Data Store (CDS) [data set], https://doi.org/10.24381/cds.adbb2d47, 2023.

Holland, D. M., and Jenkins, A.: Modeling Thermodynamic Ice–Ocean Interactions at the Base of an Ice Shelf. J. Phys. Oceanogr., 29, 1787-1800, https://doi.org/10.1175/1520-0485(1999)029<1787:MTIOIA>2.0.CO;2, 1999.

Jacobs, S. S.: Bottom water production and its links with the thermohaline circulation. Antarct. Sci., 16, 427–437, https://doi.org/10.1017/S095410200400224X, 2004.

Kang, D., and Fringer, O.: Energetics of Barotropic and Baroclinic Tides in the Monterey Bay Area. J. Phys. Oceanogr., 42, 272-290, https://doi.org/10.1175/JPO-D-11-039.1, 2012.

Legrésy, B., Wendt, A., Tabacco, I., Rémy, F., and Dietrich, R.: Influence of tides and tidal current on Mertz Glacier, Antarctica. J. Glaciol., 50, 427–435, https://doi.org/10.3189/172756504781829828, 2004.

Liu, C., Wang, Z., Liang, X., Li, X., Cheng, C., Wu, Y., Liu, Y., Yuan, X., and Yu, X.: Observed Tidal Currents in Prydz Bay and Their Contribution to the Amery Ice Shelf Basal Melting. OLAR, 2, 0020, https://doi.org/10.34133/olar.0020, 2023.

Liu,Y., Liu,C., Wang,Z., Yan,L., Haigh, M., Han,X., Liu K., Xia Y., Zeng J., Li X., Li X.: Spatial characteristics and dynamic mechanisms of the Antarctic Slope Current in the Ross Sea. J. Geophys. Res.-Oceans, 130, e2025JC023219, https://doi.org/10.1029/2025JC0232192025, 2025.

Llewellyn Smith, S. G., and Young, W. R.: Conversion of the Barotropic Tide. J. Phys. Oceanogr., 32, 1554-1566, https://doi.org/10.1175/1520-0485(2002)032<1554:COTBT>2.0.CO;2, 2002.

Losch, M., Menemenlis, D., Campin, J.-M., Heimbach, P., and Hill, C.: On the formulation of sea-ice models. Part 1: Effects of different solver implementations and parameterizations. Ocean Modell., 33, 129–144, https://doi.org/10.1016/j.ocemod.2009.12.008, 2010.

Macayeal, D.R.: Thermohaline circulation below the Ross Ice Shelf: A consequence of tidally induced vertical mixing and basal melting. J. Geophys. Res.-Oceans, 89, 597-606, https://doi.org/10.1029/JC089IC01P00597, 1984a.

MacAyeal, D. R.: Numerical simulations of the Ross Sea tides. J. Geophys. Res.-Oceans, 89, 607–615, https://doi.org/10.1029/jc089ic01p00607, 1984b.

Marshall, J., Adcroft, A., Hill, C., Perelman, L., and Heisey, C.: A finite-volume, incompressible Navier Stokes model for studies of the ocean on parallel computers. J. Geophys. Res.-Oceans, 102, 5753–5766, https://doi.org/10.1029/96jc02775, 1997.

Mazloff, M. R., Heimbach, P., and Wunsch, C.: An eddy-permitting southern ocean state estimate. J. Phys. Oceanogr., 40, 880–899, https://doi.org/10.1175/2009jpo4236.1, 2010.

Müller, M. On the space- and time-dependence of barotropic-to-baroclinic tidal energy conversion. Ocean Modell., 72, 242–252, https://doi.org/10.1016/j.ocemod.2013.09.007, 2013.

Niwa, Y., and Hibiya, T.: Estimation of baroclinic tide energy available for deep ocean mixing based on three-dimensional global numerical simulations. J. Oceanogr. 67, 493–502, https://doi.org/10.1007/s10872-011-0052-1, 2011.

Orsi, A. H., Johnson, G. C., and Bullister, J. L.: Circulation, mixing, and production of Antarctic Bottom Water. Prog. Oceanogr., 43, 55–109, https://doi.org/10.1016/S0079-6611(99)00004-X, 1999.

Ou, H.-W., Guan, X., and Chen, D.: Tidal effect on the dense water discharge, Part 1: Analytical model. Deep-Sea Res. Pt. II, 56, 874–883, https://doi.org/10.1016/j.dsr2.2008.10.031, 2009.

Padman, L., Erofeeva, S., and Joughin, I.: Tides of the Ross Sea and Ross Ice Shelf cavity. Antarct. Sci., 15(1), 31–40, https://doi.org/10.1017/S0954102003001032, 2003.

Padman, L., Fricker, H. A., Coleman, R., Howard, S., and Erofeeva, L.: A new tide model for the Antarctic ice shelves and seas. Ann. Glaciol., 34, 247–254, https://doi.org/10.3189/172756402781817752, 2002.

Padman, L., Howard, S. L., Orsi, A. H., and Muench, R. D.: Tides of the northwestern Ross Sea and their impact on dense outflows of Antarctic Bottom Water. Deep-Sea Res. Pt. II, 56(13), 818–834, https://doi.org/10.1016/j.dsr2.2008.10.026, 2009.

Padman, L., Siegfried, M. R., and Fricker, H. A.: Ocean tide influences on the Antarctic and Greenland ice sheets. Rev. Geophys., 56, 142–184, https://doi.org/10.1002/2016RG000546, 2018.

Pairaud, I. L., Auclair, F., Marsaleix, P., Lyard, F., and Pichon, A.: Dynamics of the semi-diurnal and quarter-diurnal internal tides in the Bay of Biscay. Part 2: Baroclinic tides. Cont. Shelf Res., 30, 253–269, https://doi.org/10.1016/j.csr.2009.10.008, 2010.

Pérenne, N., Pichon, A., and Huet, P.: A numerical study of stratified tidal rectification. Cont. Shelf Res., 20(1), 37–68, https://doi.org/10.1016/S0278-4343(99)00057-6, 2000.

Pillsbury, R. D., and Jacobs, S. S.: Preliminary observations from long-term current meter moorings near the Ross Ice Shelf, Antarctica. Antarct. Res. Ser., 87–107, https://doi.org/10.1029/AR043p0087, 1985.

Ray, R.: A preliminary tidal analysis of ICESat laser altimetry: Southern Ross Ice Shelf, Geophys. Res. Lett., 35, L02505, https://doi.org/10.1029/2007GL032125, 2008.

Riedel, B., Nixdorf, U., Heinert, M., Eckstaller, A., and Mayer, C.: The response of the Ekströmisen (Antarctica) grounding zone to tidal forcing. Ann. Glaciol., 29, 239–242, https://doi.org/10.3189/172756499781821247, 1999.

Rignot, E., Ciracì, E., Scheuchl, B., Tolpekin, V., Wollersheim, M., and Dow, C.: Widespread seawater intrusions beneath the grounded ice of Thwaites Glacier, West Antarctica. PNAS, 121, e2404766121, https://doi.org/10.1073/pnas.2404766121, 2024.

Robertson, R.: Baroclinic and barotropic tides in the Ross Sea. Antarct. Sci., 17, 107–120, https://doi.org/10.1017/S0954102005002506, 2005.

Robertson, R.: Tidally induced increases in melting of Amundsen Sea ice shelves. J. Geophys. Res.-Oceans, 118, 3138-3145, https://doi.org/10.1002/jgrc.20236, 2013.

Robertson, R., Beckmann, A., and Hellmer, H.: M_2 tidal dynamics in the Ross Sea. Antarct. Sci., 15, 41–46, https://doi.org/10.1017/S0954102003001044, 2003.

Robertson, R.: Internal tides and baroclinicity in the southern Weddell Sea: 1. Model description, J. Geophys. Res.-Oceans, 106, 27001–27016, https://doi.org/10.1029/2000JC000475, 2001.

Schaffer, J., and Timmermann, R.: Greenland and Antarctic ice sheet topography, cavity geometry, and global bathymetry (RTopo-2), links to NetCDF files, PANGAEA [data set], https://doi.org/10.1594/PANGAEA.856844, 2016.

Roos, P. C., and de Swart, H. E.: Tides in Coastal Seas. Influence of Topography and Bottom Friction, in: The Mathematics of Marine Modelling: Water, Solute and Particle Dynamics in Estuaries and Shallow Seas, edited by Schuttelaars, H., Heemink, A., and Deleersnijder, E., Springer, 73–102, https://doi.org/10.1007/978-3-031-09559-7, 2022.

Si, Y., Stewart, A. L., and Eisenman, I.: Coupled Ocean–Sea Ice Dynamics of the Antarctic Slope Current Driven by Topographic Eddy Suppression and Sea Ice Momentum Redistribution. J. Phys. Oceanogr., 52, 1563–1589, https://doi.org/10.1175/JPO-D-21-0142.1, 2022.

Stewart, A. L., Klocker, A., and Menemenlis, D.: Acceleration and Overturning of the Antarctic Slope Current by Winds, Eddies, and Tides. J. Phys. Oceanogr., 49(8), 2043-2074, https://doi.org/10.1175/JPO-D-18-0221.1, 2019.

Stewart, A. L., Klocker, A., and Menemenlis, D.: Circum-Antarctic shoreward heat transport derived from an eddy- and tide-resolving simulation. Geophys. Res. Lett., 45, 834–845, https://doi.org/10.1002/2017GL075677, 2018.

Tanaka, Y.: Energy Conversion Rate from Subinertial Surface Tides to Internal Tides. J. Phys. Oceanogr., 53(5), 1355-1374, https://doi.org/10.1175/JPO-D-22-0201.1, 2023.

Verdy, A., and Mazloff, M. R.: A data assimilating model for estimating Southern Ocean biogeochemistry. J. Geophys. Res.-Oceans: Oceans, 122(9), 6968–6988, https://doi.org/10.1002/2016jc012650, 2017.

https://doi.org/10.5194/egusphere-2026-2988
Preprint. Discussion started: 5 June 2026

Wang, Q., Danilov, S., Hellmer, H., and Schröter, J.: Overflow dynamics and bottom water formation in the western Ross Sea: The influence of tides. J. Geophys. Res.-Oceans, 115, C10054, https://doi.org/10.1029/2010JC006189, 2010.

Wang, C., Liu, Z., and Lin, H.: A Simple Approach for Disentangling Vortical and Wavy Motions of Oceanic Flows. J. Phys. Oceanogr., 53, 1237-1249, https://doi.org/10.1175/JPO-D-22-0148.1, 2023.

Wang, D., and Mooers, C. N. K.: Coastal-Trapped Waves in a Continuously Stratified Ocean. J. Phys. Oceanogr., 6, 853-863, https://doi.org/10.1175/1520-0485(1976)006<0853:CTWIAC>2.0.CO;2, 1976.

Weber, T., and Thomas, M.: Tidal dynamics and their influence on the climate system from the Cretaceous to present day. Glob. Planet. Change, 158, 173-183, https://doi.org/10.1016/j.gloplacha.2017.09.019, 2017.

Whitworth, T.III, and Orsi, A. H.: Antarctic Bottom Water production and export by tides in the Ross Sea, Geophys. Res. Lett., 33, L12609, https://doi.org/10.1029/2006GL026357, 2006.

Williams, R. T., and Robinson, E. S.: The ocean tide in the southern Ross Sea. J. Geophys. Res.-Oceans, 85, 6689–6696, https://doi.org/10.1029/JC085IC11P06689, 1980.

Yan, L., Wang, Z., Liu, C., Wu, Y., Qin, Q., Sun, C., Qian, J., Zhang, L.: The salinity budget of the ross Sea Continental Shelf, Antarctica. J. Geophys. Res.-Oceans, 128, e2022JC018979, https://doi.org/10.1029/2022jc018979, 2023.

Zhang, J., and Hibler, W. D.: On an efficient numerical method for modeling sea ice dynamics. J. Geophys. Res.-Oceans, 102, 8691–8702, https://doi.org/10.1029/96jc03744, 1997.

Zhang, J., and Rothrock, D.: Modeling Arctic sea ice with an efficient plastic solution. J. Geophys. Res.-Oceans, 105, 3325-3338, https://doi.org/10.1029/1999jc900320, 2000.